Available online at www.sciencedirect.com
SCIENCE DIRECT
Geochimica et Cosmochimica Acta 70 (2006) 337–363
Geochimica
www.elsevier.com/locate/gca

The mineral dissolution rate conundrum: Insights from reactive transport modeling of U isotopes and pore fluid chemistry in marine sediments

Kate Maher [a,*], Carl I. Steefel [b], Donald J. DePaolo [a,b], Brian E. Viani [c]

[a] Department of Earth and Planetary Science, 301 McCone Hall, University of California, Berkeley, CA 94720-4767, USA
[b] Earth Sciences Division, Lawrence Berkeley National Laboratory, 1 Cyclotron Road, Berkeley, CA 94720, USA
[c] Environmental Science Division, Lawrence Livermore National Laboratory, 7000 East Avenue Livermore, CA 94550, USA

Received 10 January 2005; accepted in revised form 12 September 2005

Abstract

Pore water chemistry and $^{234}U/^{238}U$ activity ratios from fine-grained sediment cored by the Ocean Drilling Project at Site 984 in the North Atlantic were used as constraints in modeling in situ rates of plagioclase dissolution with the multicomponent reactive transport code Crunch. The reactive transport model includes a solid-solution formulation to enable the use of the $^{234}U/^{238}U$ activity ratios in the solid and fluid as a tracer of mineral dissolution. The isotopic profiles are combined with profiles of the major element chemistry (especially alkalinity and calcium) to determine whether the apparent discrepancy between laboratory and field dissolution rates still exists when a mechanistic reactive transport model is used to interpret rates in a natural system. A suite of reactions, including sulfate reduction and methane production, anaerobic methane oxidation, $CaCO_3$ precipitation, dissolution of plagioclase, and precipitation of secondary clay minerals, along with diffusive transport and fluid and solid burial, control the pore fluid chemistry in Site 984 sediments. The surface area of plagioclase in intimate contact with the pore fluid is estimated to be 6.9 m^2/g based on both grain geometry and on the depletion of $^{234}U/^{238}U$ in the sediment via α-recoil loss. Various rate laws for plagioclase dissolution are considered in the modeling, including those based on (1) a linear transition state theory (TST) model, (2) a nonlinear dependence on the undersaturation of the pore water with respect to plagioclase, and (3) the effect of inhibition by dissolved aluminum. The major element and isotopic methods predict similar dissolution rate constants if additional lowering of the pore water $^{234}U/^{238}U$ activity ratio is attributed to isotopic exchange via recrystallization of marine calcite, which makes up about 10–20% of the Site 984 sediment. The calculated dissolution rate for plagioclase corresponds to a rate *constant* that is about 10^2 to 10^5 times smaller than the laboratory-measured value, with the value depending primarily on the deviation from equilibrium. The reactive transport simulations demonstrate that the degree of undersaturation of the pore fluid with respect to plagioclase depends strongly on the rate of authigenic clay precipitation and the solubility of the clay minerals. The observed discrepancy is greatest for the linear TST model (10^5), less substantial with the Al-inhibition formulation (10^3), and decreases further if the clay minerals precipitate more slowly or as highly soluble precursor minerals (10^2). However, even several orders of magnitude variation in either the clay solubility or clay precipitation rates cannot completely account for the entire discrepancy while still matching pore water aluminum and silica data, indicating that the mineral dissolution rate conundrum must be attributed in large part to the gradual loss of reactive sites on silicate surfaces with time. The results imply that methods of mineral surface characterization that provide direct measurements of the bulk surface reactivity are necessary to accurately predict natural dissolution rates.

1. Introduction

The dissolution rates of minerals in natural systems remain poorly understood. Rates measured in laboratory experiments are typically several orders of magnitude more rapid than the few available rates estimated for natural

* Corresponding author.
E-mail address: kmaher@usgs.gov (K. Maher).

0016-7037/$ - see front matter © 2005 Elsevier Inc. All rights reserved.
doi:10.1016/j.gca.2005.09.001

systems (Brantley et al., 1993; Kim, 2002; Malmstrom et al., 2000; Taylor and Blum, 1995; White et al., 1996; White and Brantley, 2003). It is not clear whether this discrepancy indicates a fundamental problem with experimental kinetic theory as applied to mineral-fluid reactions, or rather an inability to adequately characterize and account for various inhibitory effects that occur in natural systems. In this paper, we describe the application of a reactive transport model to a low-temperature natural system where there is independent information on mineral dissolution rates from isotopic data.

The differences in the overall rates of reaction measured in laboratory and field settings have been attributed to a variety of factors. These factors include limitations of reactive surface area in natural porous media (White, 1995; White and Peterson, 1990), limitations on flow and transport into low permeability zones in heterogeneous material (Drever and Clow, 1995; Malmstrom et al., 2000), the effect of reaction affinity (Kump et al., 2000; White, 1995), slow precipitation of secondary minerals (Alekseyev et al., 1997; White and Brantley, 2003), and transport rather than strict interface control of rates (Drever and Clow, 1995; Kump et al., 2000; Steefel and Lichtner, 1998). A particularly problematic aspect of dissolution rates is that they appear to decrease with the "age" of the material being weathered (Maher et al., 2004; White and Brantley, 2003). At least some of these hypotheses can be addressed through the use of multicomponent reactive transport modeling, which takes explicit account of the rate-limiting effect of slow transport, as well as incorporating mechanistic rate laws that allow individual effects on the overall rate (surface area, departure from equilibrium, inhibition or catalysis, etc.) to be considered.

A number of theories to describe mineral dissolution rates have been presented. In general, these rate laws predict that the total dissolution rate of minerals can be described with

$$\text{Rate} = A \cdot k_{\text{f}} \cdot \beta(a_i) f(\Delta G), \tag{1}$$

where A is the mineral surface area in contact with the aqueous solution, k_{f} is the rate constant (mol/m^2/s), $\beta(a_i)$ is a function or functions which describe the inhibitory or catalytic effect of dissolved species activities (e.g., pH, Al) on the rate far from equilibrium, and the last expression on the right-hand side gives the dependence of the rate on the Gibbs free energy, ΔG. Each of these terms defined in Eq. (1) has been offered as possible explanations for the discrepancy between natural and experimental rates. To explain the age dependence of dissolution rates, one must hypothesize that one or more of the variables in Eq. (1) changes systematically with time.

The actual value of the mineral surface area (m^2 mineral m^{-3} porous medium) in Eq. (1) has been proposed as one of the possible sources of the discrepancy between laboratory and field rates, although it is often a poorly defined quantity in natural field systems (White and Peterson, 1990). It is common to point out that the physical surface area need not equal the "reactive" surface area (e.g., Zhu, 2005). Most parameterizations of mineral dissolution and precipitation rates use the physical surface area, based on either gas adsorption measurements (the BET method) or geometric estimates, to calculate an intrinsic rate constant (mol/m^2 mineral/s). In these studies, therefore, the number of reactive sites per unit physical surface area of the mineral is folded into the rate constant. There are some notable exceptions to this treatment of surface area, including mechanistic dissolution models that include explicit terms to describe the effects of reactive sites, for example, via propagation of defect-generated dissolution step waves as proposed recently by Lasaga and Luttge (2001). Other mineral dissolution rate laws have been developed in which the rate depends directly on the concentration of an activated complex on the mineral surface rather than on the physical surface area (Dove, 1995; Gautier et al., 1994; Wieland et al., 1988), although such models are not always straightforward to apply in field settings. It should be noted that the number and character of reactive sites per unit surface area of a mineral may change with time, either due to aging (Van Cappellen and Qiu, 1997) or due to changes in how close to equilibrium the fluid is with respect to the reacting mineral (Blum and Lasaga, 1991; Brantley et al., 1993). Even in the absence of a measurable change in the physical surface area of reacting minerals, therefore, changes in reactivity may occur. Whether such a change in reactivity is treated as a result of the change in the number and character of reactive sites (resulting in a time-dependent rate constant), or an explicit change in the number of reactive sites per unit surface area mineral, depends on the particular formulation used.

The value of the physical surface area that is reactive can also depend on how one conceptualizes a particular system. In a dual-porosity/permeability system characterized by preferential flow paths such as fractured rock, reactive surface area in the low permeability or "immobile" regions may be technically accessible, but only via very slow diffusive transport. The reactive surface area in these immobile zones, therefore, may have a minor to negligible effect on the pore water chemistry in the mobile zones where flow is relatively rapid, thus leading to rate-limited mass transfer (Harvey and Gorelick, 2000). The reactive surface area for this system can be described as *hydrologically limited*, although some reactive transport formulations would not consider this effect explicitly in the reactive surface area term, but would treat the effect by including an additional continuum coupled to the major flow paths via slow diffusive transport (Steefel and Lichtner, 1998). A one-dimensional, single continuum reactive transport model might treat the lower reactivity of the dual porosity system, where not all of reactive surface area is equally accessible to fluid in the major flow paths, by decreasing the effective reactive surface area. These effects can be important in aquifers where the average Darcy velocity does not necessarily provide information on the detailed flow paths and possible mass transfer limitations on the rates (e.g. Zhu, 2005). At

the opposite end of the spectrum are fine-grained, uncemented, homogeneous sediments where the bulk surface area is fully accessible to the fluid. However, physical barriers such as armoring by secondary precipitates, or the development of deep surface layers, may restrict the number of available reactive sites (White and Brantley, 2003). In this case, the reactive surface area can be described as *surface limited*.

The saturation state of the mineral with respect to the fluid (defined in terms of the Gibbs free energy or reaction affinity) might also explain the difference between natural weathering rates and laboratory weathering rates and possibly even the trend of decreasing rates with weathering age. Detailed information about the saturation state of the system with respect to dissolving minerals is rarely available for most natural systems. But since many natural systems may be close to equilibrium, it is critical to know the actual dependence of the rate on the Gibbs free energy. Lasaga and Luttge (2001) suggested that the dissolution rate should show a linear dependence on the deviation from equilibrium (ΔG) only in special cases, and that a nonlinear dependence is expected where dissolution is via defect-related dissolution step waves. They supported their arguments with data from dissolution experiments conducted by Burch et al. (1993), Taylor et al. (2000), and Cama et al. (2000), although not all experiments have shown a similar dependence on the solution saturation state (Oelkers et al., 1994). The experimental rates for plagioclase measured by Burch et al. (1993) and Taylor et al. (2000) are about one order of magnitude slower under near-equilibrium conditions than predicted by a linear TST theory.

The inhibitory effect from other aqueous species, especially Al, has also been observed in experimental studies of aluminosilicate dissolution (Carroll and Knauss, 2005; Chou and Wollast, 1984; Oelkers et al., 1994). Dissolution experiments, mostly conducted far from equilibrium, have demonstrated that the dissolution of feldspar may be controlled by the formation of Al-deficient/silica-rich precursor complexes (Gautier et al., 1994; Gout et al., 1997; Oelkers et al., 1994). The degree of inhibition is proportional to the Al activity in solution. The catalytic effect of lower pH values is also well known (Chen and Brantley, 1997; Knauss and Wolery, 1986).

Although each of the above mechanisms (close-to-equilibrium conditions, Al-inhibition, and reactive surface area) can theoretically explain the apparent discrepancy between natural and laboratory rates, there has been no natural system that can be characterized sufficiently to determine to what extent the individual mechanisms explain quantitatively the discrepancies between laboratory and field rates, or the apparent age dependence of mineral reactivity. Young marine sediments may provide an in situ natural laboratory in which the factors controlling natural weathering rates can be elucidated. Deep-sea sediments have the advantage that they are fluid-saturated, are mostly uncemented, and have very high porosities (70–90%), all of which minimize limitations on the physically accessible mineral surface area. An added advantage of the deep sea sediments, particularly those below the immediate seawater-sediment interface, is that transport processes are reasonably well understood and parameterized—molecular diffusion and burial/compaction are the only significant modes of transport. In addition, physical properties like the permeability and porosity are sufficiently homogeneous that no significant preferential flow or transport develops, indicating that the reactive surface area in these sediments will be largely accessible to the fluid. They are also not subjected to rapid seasonal cycling of temperature or water content, as are soils.

The model presented here uses a coupled isotopic-geochemical reactive transport formulation to investigate the rate-controlling factors for silicate dissolution in deep-sea sediments in the North Atlantic. The U-series isotopes ^{238}U and ^{234}U, as well as the pore fluid chemical compositions, serve as independent constraints on the rates of silicate mineral dissolution and reactive surface area. The reactive transport approach has the advantage that it assumes neither strict surface reaction nor transport control, and the potential rate limitation of transport can be explicitly considered. The rates of biologic processes such as anaerobic respiration, sulfate reduction, and methanogenesis can also be determined based on reactive transport modeling of major element profiles in the pore water and serve as a biogeochemical backdrop in the analysis of the dissolution rates. Once the geochemical and biogeochemical framework is developed, the implementation of the reactive transport approach will allow us to investigate the effect of alternative rate laws and potential inhibitory mechanisms on the inferred plagioclase dissolution rate, relative to a base case set of rates and profiles. The effect of different assumptions can be assessed via the observed changes in the major element and isotopic profiles produced by the model. The goal of this analysis is to create a bridge between current kinetic and experimental theories and observations from a natural system, and identify the factors that contribute to the large discrepancy observed between laboratory and natural rates.

2. Site description

The data considered are from Ocean Drilling Project (ODP), Leg 162, Site 984A (61°25.507'N, 24°04.939'W) in the North Atlantic Ocean (Fig. 1). Site 984 is located on the Bjorn Drift on the eastern flank of Reykjanes Ridge, southwest of Iceland, at a water depth of approximately 1650 m. The sediment has an accumulation rate of about to 15.4 cm/ka from 0 to 29 m and 11.5 cm/ka from 29 to 97 m depth, and is mainly composed of well-sorted terrigenous silts derived from Iceland (Channell and Lehmen, 1999) and from more distal continental sources (DePaolo et al., in prep.).

The Site 984 core comprises a continuous sedimentary sequence from the upper Pliocene to the Holocene. The

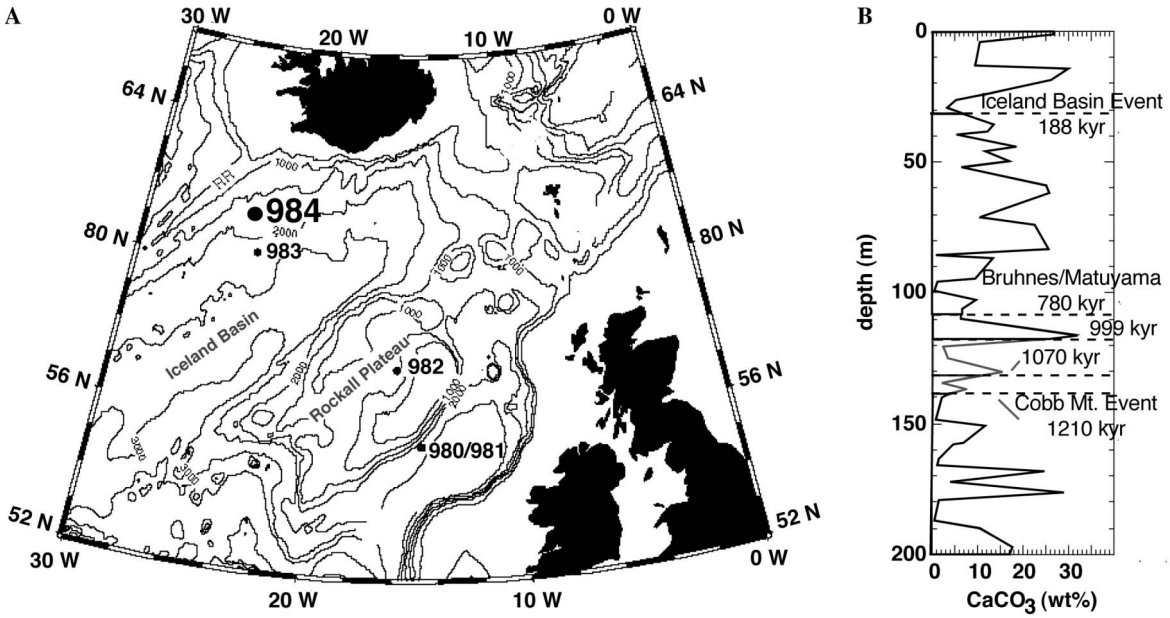

Fig. 1. (A) Location of Ocean Drilling Project Site 984 in the North Atlantic; (B) $CaCO_3$ content and age-depth constraints for Site 984 (Carter and Raymo, 1999; Channell and Lehmen, 1999).

sediments consist of four primary components: carbonate, plagioclase-rich IRD (ice-rafted debris), basaltic material derived from Iceland, and a fine amorphous component that may be biogenic silica (Carter and Raymo, 1999; Wright and Flower, 2002). Authigenic iron sulfides (commonly disseminated pyrite) are present in minor amounts. Foraminiferal abundances are quite low, hence given the difficulty in separating inorganic calcite from biogenic, only the bulk calcite is considered here. The lithology is characterized by silty clay, clay, clayey nannofossil mixed sediment, and clay with variable amounts of nannofossils and silt. The variation occurs over meters to tens of meters depth (Fig. 1).

Calcium carbonate contents were found to be between 3 and 30%, with an average of 7% (Fig. 1). The carbonate contents at Site 984 are quite variable, presumably reflective of glacial–interglacial fluctuations. The mineralogy of the sediment is dominated by plagioclase, smectite, and quartz, with lesser amounts of illite, kaolinite, and chlorite, in order of decreasing abundance (Carter and Raymo, 1999).

3. Measurements and data sources

3.1. Pore water and sediment data

Pore water samples were obtained in 10-m intervals to a depth of about 200 m (Schrag et al., 2002). Pore water samples were filtered on-ship and measured for major elements, alkalinity, and some trace elements. Samples were measured following the procedures of Murray et al. (2000) and the data are available from the ODP website (http://iodp.tamu.edu). The concentration data were converted to units of mol/kg seawater assuming a fluid density of 1.028 kg/L. The $CaCO_3$ contents, porosity, and bulk density data used in the following model were also obtained by the ODP staff during ODP leg 162.

The sediment and pore water samples for the U isotopic analyses were collected from 0.3 to 60 m depth at Site 984 A. The details of the isotopic analysis and complete results are given in Maher et al. (2004). The pore water samples were taken from near the top of the core down to ~56 m depth. U concentrations and $^{234}U/^{238}U$ ratios were measured for a sequential leach procedure modified from Tessier et al. (1979). The components measured were:

- pore water (extracted from sediment);
- exchangeable fraction (1 N MgCl leachate);
- carbonate fraction (0.1 N NaOAc leachate buffered to pH 5);
- bulk sediment (concentrated HF and $HClO_4$);
- primary silicates (residual from 1.5 N HCl leach of fresh bulk sediment).

The 1.5 N HCl leach was used to remove any primary marine minerals from the sediment to isolate the primary silicate component. This procedure was selected after remnant marine carbonate was detected in the isotopic values of the NaOAc residues. The residual samples were measured using a Micromass Isoprobe multi-collector ICP mass spectrometer at Lawrence Berkeley National Laboratory (LBNL). The remainder of the U analyses were performed at LBNL/UC Berkeley using a Micromass single collector thermal-ionization mass spectrometer and standard ion chromatography (Maher et al., 2004).

4. Multicomponent reactive transport model

The model used in this study is the Crunch multicomponent reactive transport model (Giambalvo et al., 2002; Steefel, 2001; Steefel and Lasaga, 1994; Steefel and Yabusaki, 1996). The model for Site 984 was developed by consecutively adding reaction pathways until the modeled profiles could reproduce the observed data. The stoichiometry of the overall reactions serves as an additional constraint. The parameters for the model are based on literature values, best approximations from the data, or modeling of the data. To model the marine and uranium isotopic systems, significant modifications were made, including the incorporation of fluid and sediment burial and compaction, the addition of U isotopes to the solid phases, an α-recoil parameterization, and a formulation for the co-precipitation of U into the calcite. In addition, the carbonate system was modified to be consistent with the speciation of the CO_2 system at pressures and temperatures of the deep ocean based on the thermodynamic code CO2SYS (Lewis and Wallace, 1998). These modifications are detailed in the following sections.

4.1. Solid and fluid burial

The numerical code Crunch was modified to include steady-state burial and compaction. If compaction is negligible and there is no external driving force for the fluid (such as upwelling from hydrothermal vents), then the downward advection of pore water is the same as the burial rate of solids relative to the water-sediment interface. However, compaction over long time scales in fine-grained sediments results in nonconstant pore water and solid burial rates that can produce appreciable changes in the water content, and as a consequence, the chemical profiles (Berner, 1980).

The solid burial rate, ω, can be determined from the conservation of solid sediment mass (where ϕ is the porosity and z is the depth (m)):

$$\frac{\partial[(1-\varphi)\omega]}{\partial z} = 0, \tag{2}$$

The fluid flow due to compaction, v, can be determined from the conservation of fluid mass

$$\frac{\partial(\varphi v)}{\partial z} = 0 \tag{3}$$

given the assumption of steady-state compaction and negligible porosity changes due to mineral precipitation and dissolution. Bioturbation, which affects only the top few centimeters to meters, is not considered here because of the length scale under consideration (~200 m) and the sampling interval (~2 m).

A best fit of the porosity profile as a function of the depth z for the core was achieved with a log distribution because of the large porosity changes in the upper meters

$$\varphi(z) = 0.87 - 0.089 \cdot \log(z). \tag{4}$$

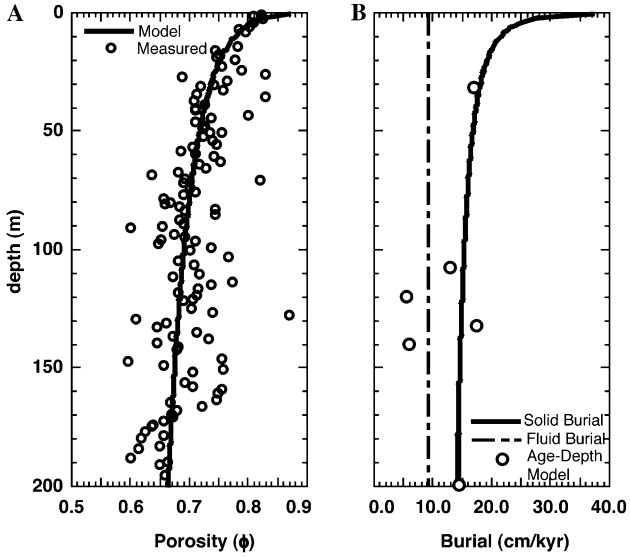

Fig. 2. Measured porosity and calculated profiles for fluid and solid burial as a function of depth; (A) measured porosity and fit to porosity data; (B) fluid and solid burial rate (cm/kyr) as used in the model. The sedimentation rates based on the depth-age constraints from Channell and Lehmen (1999) are shown in open circles. The asymptotic sedimentation rate is 14.3 cm/yr.

Using this expression for the porosity along with the asymptotic burial rate as a boundary condition at depth, solid and fluid burial rates were calculated by solving Eqs. (2) and (3) numerically using *Mathematica* (Wolfram, 2003). For Site 984, with an asymptotic burial rate of 14.3 cm/kyr, the resulting solid and fluid burial rates are shown in Fig. 2. Because solid burial rates at Site 984 have been variable over time due to changes in climate in the North Atlantic, the asymptotic burial rate from 200 m depth was used. Despite this assumption, the changes in burial rate over depth are in good agreement with the age-depth model of Channell and Lehmen (1999).

4.2. Diffusive transport

The species-specific diffusion coefficients are obtained from the literature and corrected for temperature within the model using an activation energy of 4.5 kcal/mol (Giambalvo et al., 2002 and citations contained therein; Iversen and Jorgensen, 1993; Li and Gregory, 1974). In addition to including species-specific diffusion coefficients, the reactive transport model calculates electrochemical migration based on the Nernst–Planck equation (Giambalvo et al., 2002; Van Cappellen and Gaillard, 1996), thus preserving electroneutrality.

4.3. Speciation of the CO_2 system in seawater

The speciation of inorganic carbon in seawater at 160 bar (1650 m) was taken from the values predicted by the CO2SYS program, a thermodynamic model based on stoichiometric equilibrium constants developed for seawa-

ter compositions (Lewis and Wallace, 1998). This was necessary to account for the effects of pressure, in particular, on the dissociation constants and on calcite solubility in seawater. The values of the effective equilibrium constants at 160 bar pressure that are used in the modeling are given as a function of temperature in Table 1. All carbonate species other than CO_3^{2-}, HCO_3^-, and $H_2CO_{3(aq)}$ were removed from the secondary species list in Crunch to avoid double counting of the effect of ion pairing, since this effect is included in the stoichiometric dissociation constants (K_H, pK_1, and pK_2) imported from CO2SYS. The imported stoichiometric dissociation constants are thus corrected only for the activity coefficients of the carbonate species in seawater calculated in Crunch based on the extended Debye–Hückel formulation. For the carbonate system, therefore, the treatment differs from CO2SYS only in the fact that activity coefficients based on the extended Debye–Hückel formulation are used.

The $\log K_{sp}$ for calcite used in the Crunch calculations was obtained by calibrating the saturation indices ($\log Q/K$ or $\log \Omega$) for calcite with the predictions from CO2SYS. In practice, this was done by adjusting the equilibrium constant for calcite until the saturation index ($\log \Omega$) predicted by Crunch matched that of CO2SYS for the seawater composition used as a boundary condition at the seawater-sediment interface. The $\log K_{sp}$ values for calcite as a function of temperature determined in this manner are given in Table 1. It is assumed that the calcite contains 3% Mg, a reasonable value for a marine calcite (Busenberg and Plummer, 1989). This is also the value assumed by the CO2SYS model (Lewis and Wallace, 1998). The equilibrium coefficients for the silicate minerals are not appreciably affected by the higher pressures at Site 984.

4.4. Biogeochemical reactions

The profiles that are affected by microbial processes are primarily $O_{2(aq)}$, SO_4^{2-}, NH_4^+, $CH_{4(aq)}$, and alkalinity. The biogeochemical reactions are represented by a standard set of reactions that describe aerobic respiration, sulfate reduction, and methanogenesis, coupled with secondary reactions such as the anaerobic oxidation of methane (Table 2). The organic matter is treated as a solid phase with a modified Redfield stoichiometry of $(CH_2O)_{106}(NH_3)_6(HPO_4)_{0.5}$. The ratio of C/N was increased from the standard Redfield ratio for organic matter in order to reproduce the NH_4^+ profile, following the approach of Berner (1977). A decrease in reactivity and increase in the C/N ratio of organic matter to ~17 has also been observed in other deep-sea sediments (de Lange, 1992; Wijsman et al., 2002). The rate constants for the reactions are determined in this study by fit to the sulfate, ammonia, and methane

Table 1
Dissociation and equilibrium constants for the carbonate system at 160 bar calculated using CO2SYS (Lewis and Wallace, 1998)

Parameter	Reaction	0 °C	25 °C	60 °C
pK_H	$CO_{2(g)} \leftrightarrow CO_{2(aq)}$	−1.137	−1.484	−1.755
pK_1	$CO_{2(aq)} + H_2O \leftrightarrow HCO_3^- + H^+$	−6.351	−6.164	−5.983
pK_{OW}	$OH^- + H^+ \leftrightarrow H_2O$	14.940	13.995	13.027
pK_2	$CO_3^{2-} + H^+ \leftrightarrow HCO_3$	9.946	9.595	9.234
$\log K'_{sp}$	$Ca_{0.97}Mg_{0.03}CO_3 \leftrightarrow CO_3^{2-} + 0.97Ca^{2+} + 0.03\ Mg^{2+}$	−7.530	−7.600	−7.800

Values include the activity coefficient correction.

Table 2
Reaction stoichiometry and parameters for organic matter degradation

	Reaction stoichiometry	$\log k_{max}$ (mol/m^2/s)	K_s (mol/kg)	K^{in} (mol/kg)
Mineralization reactions				
Aerobic respiration[a]	$(CH_2O)_{106}(NH_3)_6(H_3PO_4)_{0.5} + 138O_{2(aq)} \rightarrow 106CO_{2(aq)} + 122H_2O + 16HNO_3 + H_3PO_4$	−10.5[b]		
Sulfate reduction[a]	$(CH_2O)_{106}(NH_3)_6(H_3PO_4)_{0.5} + 5H^+ + 53SO_4^{2-} \rightarrow 53H_2S + 6NH_4^+ + 0.5HPO_4^{2-} + 106HCO_3^-$	−13.11[d]	0.0016[c]	1×10^{-6}[d]
Methanogenesis[a]	$(CH_2O)_{106}(NH_3)_6(H_3PO_4)_{0.5} + 51H_2O \rightarrow 6NH_4^+ + 48H^+ + 53CH_{4(aq)} + 53HCO_3^- + 0.5HPO_4^{2-}$	−13.91[d]		4×10^{-6}[d]
Secondary reactions				
Anaerobic methane oxidation	$SO_4^{2-} + CH_{4(aq)} + 2H^+ \rightarrow H_2S + CO_2 + 2H_2O$	−7.66[d,e]	0.0016[c,f] 0.010[g]	

[a] Surface area for organic matter is 0.2 m^2/m^3, from Giambalvo et al. (2002).
[b] Based on values from Giambalvo et al. (2002).
[c] The half-saturation constant for SO_4^{2-} from Wang and Van Cappellen (1996).
[d] Determined in this study.
[e] mol/L/yr.
[f] For sulfate.
[g] For methane.

profiles, but are in good agreement with previous estimates for deep-sea sediments (cf. Giambalvo et al., 2002).

The model uses multiplicative Monod kinetic rate laws to model these processes (Van Cappellen and Gaillard, 1996). The dependence of the total reaction rate (R_m) on electron donors is represented according to

$$R_m = k_{max} I_m \frac{[C_E]}{[C_E] + K_S} [OM], \quad (5)$$

where $[C_E]$ is the aqueous concentration of the limiting electron receptor, K_s is the half-saturation constant, [OM] is the concentration of organic matter, and k_{max} is the maximum rate of the reaction when $C_E \gg K_s$ (Soetaert et al., 1996; Wijsman et al., 2002). For methanogenesis, the oxidation of carbon may also be inhibited by the presence of other oxidants that are more favorable, in this case sulfate (Cagatay et al., 2001; Hunter et al., 1998; Wijsman et al., 2002). The inhibition of methanogenesis due to sulfate concentration is modeled as

$$I_m = \left(\frac{K^{in}_{SO_4}}{[SO_4^{2-}] + K^{in}_{SO_4}} \right), \quad (6)$$

where $K^{in}_{SO_4}$ is the inhibition constant (i.e., the concentration of sulfate above which methanogenesis is inhibited). A similar formulation applies to the inhibition of sulfate reduction by O_2, although this effect is minor because of very low O_2 concentrations below about 1 m depth. The parameter values for aerobic respiration, sulfate reduction, and methanogenesis are listed in Table 3.

4.5. Minerals and associated reactions

4.5.1. $Fe(OH)_3$ and $H_2S_{(aq)}$

The redox processes, most mediated by bacteria, lead to an accumulation of both aqueous $CO_{2(aq)}$, NH_4^+, and $H_2S_{(aq)}$, and solids such as iron sulfide. The dissolution of Fe(III)-oxides by $H_2S_{(aq)}$ prevents the accumulation of pore water sulfide created during biologic SO_4^{2-} reduction (Wang and Van Cappellen, 1996). The presence of sulfide in the pore water leads to the formation of amorphous FeS, which then reacts with native sulfur to form pyrite (Yao and Millero, 1996). Because there were no data for Fe in the pore water available, or Fe bearing phases (only anecdotal evidence of pyrite exists), the amount of $Fe(OH)_3$ or FeS is unknown. The burial flux of $Fe(OH)_3$ was set so as to produce a concentration consistent with other marine deposits (ca. Giambalvo et al., 2002). The burial flux of pyrite is assumed to be zero. Since the formation of these minerals has important effects on the alkalinity and pH of the system through the removal of $H_2S_{(aq)}$ from solution, it was important to include them in the reaction network, despite the relatively few constraints on their composition and abundance for Site 984. The rates of the H_2S reaction with Fe-oxyhydroxide were set such that H_2S remained low (in the micromolar range) throughout the sediment column.

4.5.2. Silicate minerals

The Site 984 sediments are composed of plagioclase, smectite, illite, and kaolinite in order of decreasing abundance (Raymo et al., 1999). Precise mineralogical abun-

Table 3
Reaction stoichiometry and structural formulas for principal reactions

Mineral	Reaction stoichiometry or mineral formula	log k (mol/m^2/yr)	log K (25 °C)[a]	Volume fraction (m^3/m^3)	Surface area
Minerals					
Calcite	$CaCO_3 + H^+ \leftrightarrow Ca^{2+} + HCO_3^-$	−6.19[b]	−7.62[c]	0.04	1.0 m^2/m^3
$SiO_{2(am)}$	$SiO_{2(am)} \leftrightarrow SiO_{2(aq)}$	−11.0[c]	−2.71	0.02	1.0 m^2/m^3
$FeS_{(am)}$	$FeS_{(am)} + H^+ \leftrightarrow Fe^{2+} + HS^-$	−9.0[d]	−4.65	0.0	0.2 m^2/m^3
Pyrite	$0.25H^+ + 0.25SO_4^{2-} + Fe^{2+} + 1.75HS^- \leftrightarrow FeS_2 + H_2O$	−10	24.65	0.0	1.0 m^2/m^3
$Fe(OH)_3$	$Fe(OH)_3 + 0.5H_2S \leftrightarrow Fe^{2+} + H_2O + 2OH^- + 0.5S°$	−6.00[d,e]	−11.60	0.02	0.25 m^2/m^3
Siderite	$Fe^{2+} + 1.0HCO_3^- \leftrightarrow FeCO_3 + H^+$	−10	−0.228	0.0	1.0 m^2/m^3
Silicate minerals					
Plagioclase	$Ca_{0.497}Na_{0.5}U^{234}_{10^{-10.25}}U^{238}_{10^{-5.95}}Al_{1.5}Si_{2.5}O_8$	Variable	14.30	0.04	6.9 m^2/g
Smectite	$Ca_{0.025}Na_{0.1}Fe(III)_{0.20}Fe(II)_{0.50}K_{0.2}Al_{1.15}Si_{3.5}O_{10}(OH)_2$	−18.50 ± 1.5[f]	17.42	0.08	55 m^2/g
Sepiolite	$Mg_4Si_6O_{15}(OH)_2{\cdot}6H_2O$	−19.00 ± 1.5[f]	30.44	0.01	55 m^2/g
Kaolinite	$Al_2Si_2O_5(OH)_4$	−19.00 ± 1.5[f]	6.81	0.01	55 m^2/g
Illite (I/S)[g]	$Ca_{0.01}Na_{0.01}Fe(III)_{0.36}Mg_{0.44}K_{0.53}Si_{3.55}Al_{1.72}O_{10}(OH)_2$	−19.00 ± 1.5[f]	6.58	0.01	55 m^2/g

[a] The standard state adopted in this study is that of unit activity for pure minerals and H_2O at any temperature and pressure. For aqueous species other than H_2O, the standard state is unit activity of the species in a hypothetical 1 molal solution referenced to infinite dilution at any temperature and pressure. Equilibrium constants used in these calculations were taken from the EQ3/6 database (Wolery et al., 1990), with the exception of the illite (I/S) and the carbonate system in Table 1. The sensitivity of the simulation results was tested in some cases by varying the log K for plagioclase and the clay minerals (see Sections 6.3 and 6.4).

[b] Lei et al. (1989).

[c] Determined using CO2SYS program of Lewis and Wallace (1998) at 160 bar.

[d] Giambalvo et al. (2002).

[e] Based on Yao and Millero (1995).

[f] Determined this study for base case.

[g] Illite composition and equilibrium coefficient used are based on the study by Kohler et al. (2003) for a mixed layer illite/smectite clay, the Illite du Puy. This composition was chosen because no data exists for the composition/thermodynamic considerations of authigenic illite in the North Atlantic.

dances are not available due to the difficulty in converting XRF data to relative abundance, however, estimates of the relative fraction were made based on the peak intensity for each mineral and a correction factor from Biscaye (1965). Because the sediments are primarily derived from Iceland, they were assumed to be made up primarily of plagioclase feldspar. A mid-range 50:50 anorthite:albite composition was used. The clays observed in the core were primarily smectite, with lesser amounts of illite and kaolinite.

The array of minerals found at Site 984 and the observed pore water profiles suggest that authigenic mineral precipitation may be occurring within the young North Atlantic sediments. The formation of authigenic clays in young marine sediments is difficult to assess because of the high detrital clay component typically associated with marine deposits. Recent field and experimental studies have demonstrated that appreciable precipitation of illite, smectite, and kaolinite occurs in the early stages of diagenesis and at low temperatures (ca. 3–25 °C) (Cole, 1985; Karpoff et al., 2002; Mackin and Aller, 1986; Michalopoulos and Aller, 1995, 2004). The decreasing K/Cl and Mg/Cl ratios and increasing Na/Cl ratios in pore water from Site 984 also suggest that the K^+ and Mg profiles are a result of secondary clay precipitation. The composition of the silicate minerals and related parameters are included in Table 3.

4.6. Kinetic rate law formulations

As a base case, the dissolution and precipitation kinetics used in the model are described as reversible reactions with a linear dependence on the deviation from equilibrium (or the saturation state, Ω), often referred to as a linear TST (Transition State Theory) rate law. However, we also consider rate law formulations that include a nonlinear dependence on mineral saturation state (Burch et al., 1993) and inhibition by aqueous aluminum (Carroll and Knauss, 2005; Gautier et al., 1994; Oelkers et al., 1994).

4.6.1. Close-to-equilibrium rate law

Some dissolution experiments performed near equilibrium ($\log\Omega > -5$) have shown that the kinetic behavior of minerals may deviate from the standard linear kinetic formulation (Alekseyev et al., 1997; Burch et al., 1993; Nagy et al., 1991). Burch et al. (1993) presented data on albite dissolution that indicated an abrupt increase in the dissolution rate beyond a region of critical undersaturation. They attributed these data to a change in the nature of dissolution from etch-pit formation under far from equilibrium conditions to uniform surface lowering under close to equilibrium conditions (Burch et al., 1993; Lasaga et al., 1994). These data suggest that in the case of albite, a linear TST formulation using a rate constant determined far from equilibrium would overpredict rates close to equilibrium by about an order of magnitude.

Although various interpretations of the data in Burch et al. (1993) are possible, we test the effect of such nonlinear dependences on the degree of undersaturation by using two

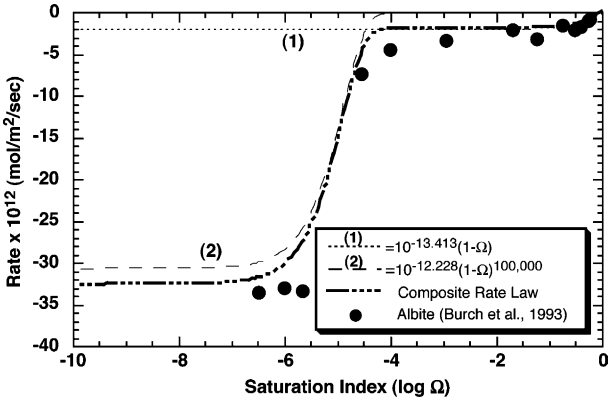

Fig. 3. Model fit to albite data of Burch et al. (1993) showing the composite rate and the individual parallel rate laws.

parallel rate laws, one a linear TST model that captures the close to equilibrium behavior

$$R_1 = A \cdot k_1(1-\Omega)^1 \tag{7}$$

and a second nonlinear rate law for the "far-from-equilibrium" realm

$$R_2 = A \cdot k_2(1-\Omega)^{100{,}000}, \tag{8}$$

where the rate constants k_1, k_2 and the exponent are fitted from the Burch et al. (1993) data shown in Fig. 3.

4.6.2. Aluminum inhibition model

Far from equilibrium experiments have suggested that aluminosilicate dissolution rates are controlled by the formation and decomposition of an Al-deficient, silica-rich surface precursor complex (Carroll and Knauss, 2005; Gautier et al., 1994; Oelkers et al., 1994). The reaction for the overall removal of Al from the hydrogenated feldspar to form a silica-rich precursor complex M–$SiOH_{3n}$ is described by Oelkers et al. (1994), rewritten here in terms of the aqueous species $Al(OH)_3$ instead of Al^{3+}, as

$$\text{M–}n\text{AlSiO} \Longleftrightarrow \text{M–SiOH}_{3n} + \text{nAl(OH)}_n, \tag{9}$$

where n is the number of moles of Al in the surface site M–*nAlSiO* complex (see Appendix 2 for complete derivation and discussion). As discussed by Wieland et al. (1988), the rate of dissolution far from equilibrium can be written in terms of a rate constant multiplied by the concentration of a precursor species, in this case the silica-rich surface complex

$$r_+ = k_+(\text{M–SiOH}_{3n}). \tag{10}$$

This kinetic expression can be rewritten in terms of aqueous species and the total number of reactive sites by making use of the law of mass action for Eq. (9) and the fact that the Al-rich and Si-rich surface complexes must add up to the total number of reactive sites, S, such that

$$S = [\text{M–}n\text{AlSiO}] + [\text{M–SiOH}_{3n}]. \tag{11}$$

Combining these equations, the concentration of the Al-rich surface complex can be eliminated to give

$$\mathrm{M\text{–}SiOH}_{3n} = \frac{K'_{\mathrm{f}}(S - \mathrm{M\text{–}SiOH}_{3n})}{[\mathrm{Al(OH)_3}]^n}, \tag{12}$$

where K'_{f} is the equilibrium constant for the reaction in Eq. (9). Factoring out the concentration of the Si-rich precursor complex would yield an expression equivalent to that derived by Oelkers et al. (1994). Gautier et al. (1994). It may also be expressed by multiplying by the concentration of $Al(OH)_3$, which after rearranging, then yields a rate expression of the form (see also Appendix 2, Eq. (A.4))

$$r_+ = k_+ S \frac{K'_{\mathrm{f}}}{\left([\mathrm{Al(OH)_3}]^n + K'_{\mathrm{f}}\right)}. \tag{13}$$

This equation makes clear the hyperbolic form of the aluminum inhibition term, which is mathematically similar to the inhibition terms used commonly in microbial kinetics (e.g., Eq. (5)). Note that when combined with an appropriate distribution of species calculation, as is carried out in the reactive transport calculations, Eq. (13) can be recast implicitly in terms of total dissolved aluminum (Appendix 2). Taking the value of $n = 1/3$, as determined by Carroll and Knauss (2005), and multiplying the rate constant per unit precursor sites, k_+, by the total number of sites, S, to obtain the intrinsic rate constant in terms of the total mineral surface area, k_{f}, the overall rate becomes

$$R = A \cdot k_{\mathrm{f}} \frac{K'_{\mathrm{f}}}{K'_{\mathrm{f}} + a^{1/3}_{\mathrm{Al(OH)_3}}} \left(1 - \Omega^{1/3}\right), \tag{14}$$

A $\log K'_{\mathrm{f}}$ value of -4.824 was derived from the data of Carroll and Knauss (2005) after rewriting the reaction for the formation of the Si-rich precursor in terms of $Al(OH)_3$ rather than in terms of Al^{3+} as they did. The intrinsic rate constant (k_{f}) value $10^{-12.7696}$ mol/m^2/s, the product of the rate constant per unit precursor sites, k_+, and the total number of sites, S, is also taken from Carroll and Knauss (2005). This formulation also includes a 1/3 dependence on saturation state, with the value of 1/3 corresponding to Temkin's average stoichiometric number equal to the ratio of the rate of destruction of the precursor complex and the overall dissolution rate (Gautier et al., 1994).

4.7. Uranium-series disequilibrium model

4.7.1. Bulk dissolution rates from $^{234}U/^{238}U$ in fluid and solids: theory

The U-series isotopes of ^{234}U and ^{238}U can serve as an indicator of in situ dissolution rates in natural systems. In silicate rocks and minerals, the ^{234}U/^{238}U activity ratio is equal to the secular equilibrium value of 1.0. The energetic α-decay of ^{238}U causes the grain to preferentially lose ^{234}Th (which decays rapidly to ^{234}U). This process results in solid ^{234}U/^{238}U values lower than secular equilibrium, depending on the age and size of the fragment (Fleischer, 1982, 1988; Hussain and Krishnaswami, 1980; Kigoshi, 1971). The α-recoil displacement of the ^{234}Th in a silicate is approximately 30 nm, thus for small fragments with a high surface area to volume ratio this depletion can be quite high—of the order of 10% for a spherical particle 10 μm in diameter. The uranium data for the residual solids from Site 984 clearly show evidence of this depletion (Fig. 4A).

The loss of ^{234}Th and immediate production of ^{234}U results in substantial increases in the ^{234}U/^{238}U value of the fluid in contact with the grain. The pore waters at Site 984 show an increase in ^{234}U/^{238}U with depth from the marine value of ~1.149 to a value of 1.4–1.6 (Fig. 4A). Conversely, weathering of the solid releases uranium to the fluid at the ^{234}U/^{238}U value of the weathering solid, which is ≈0.9. The unique aspect of this approach is that the pore water reflects a balance between the rate of the α-recoil process and the dissolution of the mineral. The residual solid, in contrast, only shows the effect of the α-recoil loss.

The calculated weathering rate of the solids from the U-series isotopes is then a function of the balance between the α-recoil loss fraction (f_α) and the difference between the activity ratios of the weathering solid and the fluid. To a good approximation, the reaction rate for the solid phase is determined from the pore fluid and solid isotopic ratios by (Maher et al., 2004)

$$k_{\mathrm{U}}(\mathrm{mol/m^2/s}) = \frac{\lambda_{234}}{(A)(\mathrm{GFW})} \frac{f_\alpha}{(r_{\mathrm{f}} - r_{\mathrm{s}})}, \tag{15}$$

where GFW is the gram formula weight of the dissolving species, f_α is the α-recoil loss fraction, λ_{234} is the decay constant for ^{234}U (8.96×10^{-14} s^{-1}), and r_{f} and r_{s} are the ^{234}U/^{238}U activity ratios for the fluid and the solid, respectively. Substituting for A (6.9 ± 1.5 m^2/g), GFW of feldspar (270 g/mol), $r_{\mathrm{f}}(1.4)$, $r_{\mathrm{s}}(0.9)$, and $f_\alpha(0.14 \pm 0.03)$ gives a rough value for bulk dissolution rate of plagioclase (normalized to the surface area) of $10^{-16.9\pm0.9}$ ($1.3 \pm 0.95 \times 10^{-17}$) mol/m^2/s (Maher et al., 2004). No ΔG or catalytic/inhibitory effects are considered in this calculation.

4.7.2. Physical surface area from $^{234}U/^{238}U$ depletion in solids

Surface areas measured on fresh bulk sediment from Site 984A by the BET method (N_2 gas adsorption) average 55 m^2/g. This value is presumed to reflect primarily the clay surface area, since clay minerals tend to have large specific surface areas and comprise a significant fraction of bulk solids (Table 3). The surface area of the plagioclase is much less certain. However, the ^{234}U/^{238}U in the residual solids provides a unique constraint on the reactive surface area of the sediments because the α-recoil loss fraction (f_α) is a function of the ratio of surface area to volume. The depletion of ^{234}U is confined to a surface layer 30 nm in length, the approximate stopping distance of ^{234}Th in a feldspar. The relationship between the α-recoil loss fraction (f_α) and surface area (A) is (Kigoshi, 1971; Luo et al., 2000)

$$f_\alpha = \frac{1}{4} L \cdot A \cdot \rho_{\mathrm{s}}, \tag{16}$$

where L is the stopping distance (30 nm) and ρ_{s} is the density. Based on measurement of ^{234}U/^{238}U in residual solids,

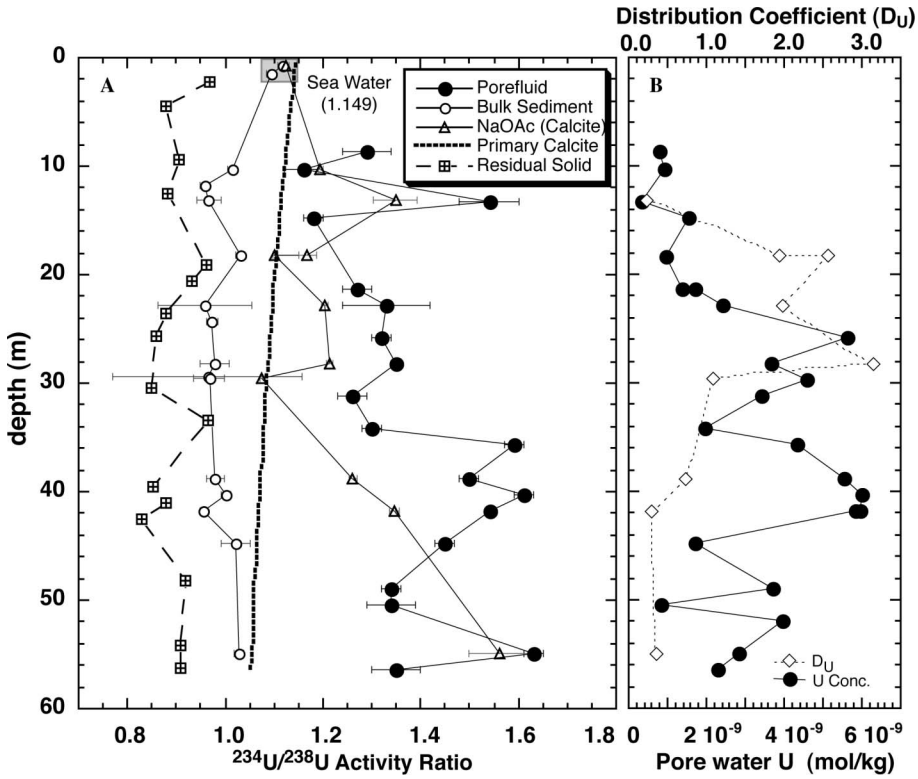

Fig. 4. U isotopic profiles and calculated distribution coefficient for Site 984. (A) $^{234}U/^{238}U$ activity ratios for pore fluid, bulk solid leachates, and insoluble residue. Dashed line is the activity ratio that corresponds to the evolution of primary marine calcite formed with the initial seawater $^{234}U/^{238}U$ activity ratio of 1.149 and *no* incorporation of new pore water U (i.e., no precipitation or recrystallization). (B) pore water uranium concentrations and calculated distribution coefficient for U in calcite. Initial values are quite high most likely due to low uranium concentrations in the pore water. The average value is 1.4.

f_α is estimated to be between 0.11 and 0.17 (Maher et al., 2004). Given this estimate of the α-recoil loss fraction, the amount of surface area in contact with the pore fluid can be constrained. The surface area of the feldspars is estimated by this method at between 5.4 and 8.4 m^2/g (Fig. 5). To produce the observed levels of ^{234}U depletion in the solids requires that the surface area of plagioclase be at least 8.4 m^2/g, with a best estimate of 6.9 m^2/g. These values are also consistent with a geometric estimate based on the mean grain size of 5–10 μm and a surface roughness factor (λ, where λ = physical surface area/geometric surface area) of ~20, in a similar range to roughness factors in natural systems (Hochella and Banfield, 1995; White, 1995).

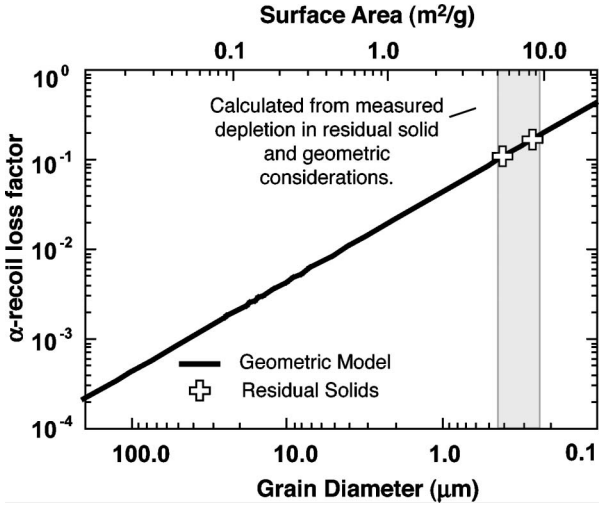

Fig. 5. Physical surface area calculated from the α-recoil loss fraction (f_α) for primary residual solids at Site 984 and Eq. (16).

4.7.3. Co-precipitation and recrystallization of uranium in calcite

The $^{234}U/^{238}U$ of the NaOAc leaches, which reflect the carbonate fraction of the sediment, also show an increase with depth (Fig. 4). The values fall between the primary expected marine calcite and the pore water. Authigenic calcite forms with the activity ratio of the pore water (Henderson and Onions, 1995; Ku, 1976; Richter and DePaolo, 1987; Richter and Liang, 1993; Robinson et al., 2004; Thomson et al., 1990), thus the bulk calcite represents a combination of newly precipitated and primary marine carbonate.

From the data, we also infer that "recrystallization" of calcite is occurring via a dissolution and re-precipitation mechanism. The bulk calcite isotopic values approach the pore water values at 60–70 m depth, suggesting that the calcite has exchanged uranium with the pore water—the isotopic values are too high to be generated by precipitation

alone. The data suggest that by 55–60 ms depth, the calcite may be more than 20–30% recrystallized.

The processes of recrystallization and precipitation are distinct from one another and must be treated differently in the numerical model. Precipitation depends on the fluid composition and the Gibbs free energy (ΔG) of the reaction. The precipitation of uranium with calcite does not affect the activity ratio of the pore fluid, although it does affect the total uranium in solution.

Recrystallization can take place even if the pore fluid and the mineral are nominally at equilibrium. As a largely isochemical process, it does not affect the major element chemistry of the pore fluid if the dissolution rate and the precipitation rate are equal. However, the isotopic composition of the pore fluid and the mineral, and the total concentration of uranium, can be affected. Recrystallization may be driven by the system's tendency to minimize the interfacial free energy via Ostwald ripening (Hover et al., 2002; Steefel and Van Cappellen, 1990) or by undetectable small departures from chemical equilibrium, neither of which is treated explicitly in the numerical model. The dissolution step of recrystallization affects the isotopic composition of the pore fluid, because the dissolving calcite may have a different isotopic composition than the pore fluid. The precipitation step of recrystallization does not affect the isotopic ratio of the pore fluid, but does affect the total uranium in solution. When the calcite is recrystallized, the U in the original calcite is exchanged with the U dissolved in the pore water

$$\mathrm{Ca}\left(^{234}\mathrm{U}/^{238}\mathrm{U}\right)_{\mathrm{marine}}\mathrm{CO_3} \xrightarrow{k_r} \mathrm{Ca}\left(^{234}\mathrm{U}/^{238}\mathrm{U}\right)_{\mathrm{pw}}\mathrm{CO_3}, \tag{17}$$

where k_r is the irreversible rate of recrystallization and the subscripts represent original (marine) and the recrystallized stoichiometry reflective of the local pore water value (pw). Since the pore water U activity ratio for Site 984A is much higher than that of marine calcite (Fig. 4A), exchange with the pore water progressively enriches the bulk calcite in ^{234}U, while lowering the activity ratio of the pore fluid.

Both the process of recrystallization and precipitation are modeled using a distribution coefficient that describes the partitioning between the aqueous and solid phases. For example, uranium partitioning between calcite and the aqueous solution can be described as

$$D_{\mathrm{U}} = \frac{X_{\mathrm{U}}[\mathrm{Ca}^{2+}]}{X_{\mathrm{Ca}}[\mathrm{UO}^{2+}]}, \tag{18}$$

where $[\mathrm{UO}^{2+}]$ and $[\mathrm{Ca}^{2+}]$ are the molar concentrations of the trace element and calcium ions in the aqueous solution, and X_{U} and X_{Ca} represent the molar fractions of U and Ca in the calcite, and D_{U} is the distribution coefficient (Lakshtanov and Stipp, 2004; Meece and Benninger, 1993). When $D_{\mathrm{U}} > 1$, the crystal is enriched in uranium relative to the solution, and for values of $D_{\mathrm{U}} < 1$, the crystal is depleted in uranium. Experimental distribution coefficients for U co-precipitation in marine calcite from seawater at 25 °C and 1 atm range from 0.2 to 10 (Meece and Benninger, 1993). Distribution coefficient values calculated from the Site 984 data suggest values of between 3.1 and 0.3 with an average value of 1.4, which agree with other estimates of D_{U} for authigenic marine carbonate (Teichert et al., 2003).

4.7.4. U-series model architecture

To use the U-series isotopes as an additional model constraint, the reactive transport model is modified to include ^{234}U and ^{238}U by considering the following processes:

(i) decay of total ^{234}U and ^{238}U (i.e., U in the solid and fluid phases);
(ii) dissolution of plagioclase with an average activity ratio of 0.9;
(iii) dissolution of marine $CaCO_3$ with isotopic composition of seawater;
(iv) co-precipitation of U with $CaCO_3$ at the isotopic value of the local pore fluid;
(v) α-recoil supply of ^{234}U to the pore fluid as a function of the α-recoil loss fraction, f_α, and the concentration of ^{238}U in the mineral, and
(vi) isotopic exchange of marine calcite with the pore fluid as a result of recrystallization.

The two uranium isotopes under consideration are represented in the model as individual species. The model presented here considers only total uranium in order to be consistent with the distribution coefficient formulation. Since it is unlikely that any pure uranium phase is precipitating or dissolving, the uranium is presumably distributed as a trace element in the individual minerals. Table 4 lists

Table 4
Composition of U minerals

Mineral	Formula	Rate (mol/m^2/s)
Plagioclase[a]	$Ca_{0.497}Na_{0.5}U^{234}_{10^{-10.25}}U^{238}_{10^{-5.95}}Al_{1.5}Si_{2.5}O_8$	Variable
Marine calcite[b]	$Ca_{0.97}Mg^{234}_{0.03}U^{238}_{10^{-10.28}}U_{10^{-6.08}}CO_3$	$10^{-6.19}$[c]
Recrystallized calcite	$Ca_{0.97}Mg^{234}_{0.03}U^{238}_{\mathrm{variable}}U_{\mathrm{variable}}CO_3$	$10^{-10.6}$[d]
α-recoil	^{234}U	$10^{-27.63}$[e]

[a] Corresponds to U concentration of 1 ppm and solid ^{234}U/^{238}U activity ratio of 0.90 (Maher et al., 2004).
[b] Corresponds to U concentration of 2 ppm and ^{234}U/^{238}U activity ratio of 1.149.
[c] Lei et al. (1989).
[d] Determined this study, with instantaneous composition depending on the local pore water composition.
[e] Corresponds to f_α of 0.14 and RSA of 6.9 m^2/g (Maher et al., 2004).

the assumed stoichiometry for the two isotopes in the solid and fluid phases. Because the amount of U co-precipitated with the calcite is quite small, it has a negligible effect on the solubility.

Radioactive decay of both isotopic species is allowed to occur in both the fluid and the solid phases. The process of α-recoil loss to the fluid is parameterized by a bulk ^{234}U supply rate, F_α

$$F_\alpha = \frac{f_\alpha \lambda_{238} C_s}{A}, \quad (19)$$

where f_α is the α-recoil loss fraction (Eq. (16)), λ_{238} is the decay constant for ^{238}U (1.55×10^{-10} yr^{-1}), A is the surface area, and C_s is the number of ^{238}U atoms in the solid. The α-recoil term is treated as a solid phase reaction that provides ^{234}U to the pore water at a defined rate. This equation predicts α-recoil rates between $10^{-27.48}$ and $10^{-27.79}$ mol $^{234}U/m^2/s$ (≈0.0003 atoms/m^2/s) for a solid U concentration of 1.0 ppm (Maher et al., 2004).

4.8. Model conditions and parameters

The model domain consists of a one-dimensional column of sediment with a Dirichlet-type boundary condition (constant concentration) for dissolved species and a prescribed flux boundary condition for solids at the sediment–sea water interface, and a no flux boundary condition at the bottom (200 m depth). A constant grid spacing of 1 m was used. The boundary conditions at the sea water–sediment interface incorporate the modern seawater composition and a combination of inferred and measured solid phase compositions (Langmuir, 1997; Lewis and Wallace, 1998). There are several important components in the marine system that were not measured in the Site 984 pore waters, most notably Al, H_2S, $B(OH)_3$, and Fe. Seawater values of Langmuir (1997) were assumed to be representative of seawater values for elements where site-specific values were not available. A summary of the boundary conditions is shown in Table 5.

Each model scenario was run for two million years, the approximate age of the sediments at 200 m depth, to achieve a steady state. The process of ion exchange is not considered. Ion exchange concentrations can reflect local pore water chemistry in a steady-state system. However, this effect is significant only when sediment burial is much more rapid than observed at Site 984 (Giambalvo et al., 2002). A linear thermal gradient of 0.105 °C/m was used to calculate temperature-dependent equilibrium constants given measured temperatures of 8 °C at 27 m depth and 24 °C at 180 m depth (Carter and Raymo, 1999). The temperature dependence of the equilibrium constants, and diffusion coefficients was calculated following the formulation described in Giambalvo et al. (2002).

Table 5
Boundary conditions for reactive transport model at the sediment–water interface

Sea water[a]	Boundary conditions		
	Concentration (mol/kg)	Sediment	Burial flux (mol/cm^2/yr)
pH	8.15	Calcite	3.02×10^{-5}
$CO_{2(aq)}$	2.30×10^{-3}	Smectite	2.14×10^{-5}
$O_{2(aq)}$	1.80×10^{-4}	Plagioclase	1.35×10^{-5}
Al^{3+}	3.85×10^{-8}[b]	$Fe(OH)_3$	4.35×10^{-6}
Ca^2	1.03×10^{-2}	Kaolinite	3.74×10^{-6}
K	1.20×10^{-2}	Sepiolite	1.31×10^{-6}
Fe	2.60×10^{-8}[c]	Illite	7.44×10^{-7}
H_2S	1.00×10^{-15}	Organic carbon	2.98×10^{-7}
Mg^{2+}	5.11×10^{-2}	FeS	0
Na^+	4.74×10^{-1}	Siderite	0
NH_4^+	1.48×10^{-9}	Pyrite	0
NO_3^-	39.2×10^{-9}		
PO_4^-	2.70×10^{-5}		
$SiO_{2(aq)}$	5.55×10^{-4}		
SO_4^{2-}	2.81×10^{-2}		
^{238}U	1.34×10^{-09}[d]		
^{234}U	8.50×10^{-14}[e]		
$B(OH)_4$	4.00×10^{-4}		

[a] Concentrations are for average seawater (Langmuir, 1997) unless otherwise noted.
[b] From Hall and Measures (1998). Al measurements in deep-sea pore waters are commonly below detection limits.
[c] Assumed to be all primarily Fe(II).
[d] From pore water concentrations in the upper 1 m of the core.
[e] Corresponds to seawater activity ratio of 1.149 (Delanghe et al., 2002).

5. Results

5.1. Organic matter degradation

The concentration profiles affected by microbial processes are primarily SO_4^{2-}, NH_4^+, $CH_{4(aq)}$, and the alkalinity (Fig. 6 and Fig. 7). The dissolved oxygen is depleted at one meter depth by aerobic respiration. These profiles reflect a common diagenetic sequence of sulfate reduction followed at depth by methanogenesis. The SO_4^{2-} concentrations of the pore water at Site 984 decrease from 26.8 mmol/kg to approximately zero by 200 m depth, coincident with an increase in NH_4^+ values (Fig. 7). Methanogenesis occurs deep in the sediment column (below 120 m) and at sulfate concentrations less than about 0.3 mmol/kg, which is most likely the concentration at which the methanogenic pathway becomes more favorable. Methane values reach a peak of 700 μmol/kg at 300 m. The sharp increase of methane with depth, and the decrease in sulfate beyond what can be attributed to sulfate reduction, suggest that anaerobic oxidation of methane by sulfate is occurring between about 100 and 150 m depth (Fig. 6).

Most of the rate constants in the literature for methane oxidation, sulfate reduction, and methane production are determined from near-shore or shallow marine environments. The rate of sulfate reduction in the model was adjusted to achieve the best fit to the sulfate profile, and the ratio of C/N was increased to fit the ammonia data (Table 2). This is a similar approach to the models of Berner (1977) and de Lange (1992), which proposed that the C/N ratio of the organic matter can be determined from the gradient in the sulfate and ammonia profiles. The relatively

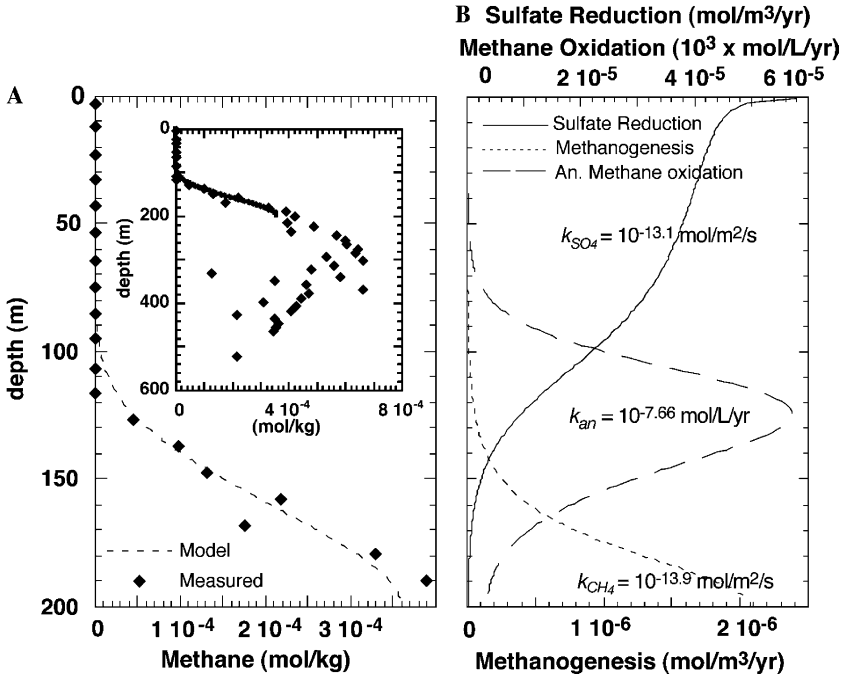

Fig. 6. Rates of anaerobic microbial degradation of organic matter. (A) modeled and observed methane concentrations. (B) rates of sulfate reduction (k_{SO_4}), methanogenesis (k_{CH_4}), and anaerobic methane oxidation (k_{an}).

slow rates of sulfate reduction, and the extended depth over which sulfate reduction occurs are consistent with the high C/N ratio inferred for the organic matter. Similar profiles and C/N values have been observed elsewhere in the North Atlantic and are presumed to reflect a more refractory organic matter composition (Cagatay et al., 2001; de Lange, 1992).

The rate of methanogenesis was also determined by fit to the methane data, and the rate of methane re-oxidation by sulfate was determined as the minimum rate required to reduce the methane concentrations in the upper profile with minimal effects on the $H_2S_{(aq)}$. Fig. 6 shows the methane concentrations and the rates of concurrent reactions. If methane oxidation were not occurring, the point where the sulfate and methane profiles intersect would occur at shallower depth and the gradient of the methane front would become much less steep because of upward methane diffusion.

5.2. Major element, pH, and alkalinity profiles

The calculated and measured profiles for selected major elements, pH, and alkalinity are shown in Fig. 7, and the corresponding model parameter values are provided in Table 3. The profiles of Fig. 7, and the calculated rate constants, comprise the base case scenario using a linear TST rate law formulation (Eq. (1) with $f(\Delta G) = 1 - \Omega^1$). The majority of the calculated profiles are in good agreement with the data to the full depth of 200 m for a dissolution rate constant value of $10^{-18.0\pm0.9}$ mol/m^2/s and a surface area of 6.9 m^2/g. The microbial reactions involving sulfate, ammonia, and methane are important for the silicate and carbonate reaction network because they produce a large amount of bicarbonate, thereby generating sufficient carbonate alkalinity to drive calcite precipitation. The calcite precipitation in turn is then controlled by the supply of dissolved Ca^{2+}. The Ca^{2+} decreases markedly in the upper 70 m of the profile, coincident with an increase in the alkalinity. The Ca^{2+} increases again below 120 m as sulfate reduction decreases. In the absence of silicate mineral dissolution, the model predicts that the Ca would be nearly consumed in the upper few meters of the core. The only way to maintain the observed Ca^{2+} levels is to have concurrent dissolution of a calcium-bearing silicate mineral. For K^+ and Mg^{2+}, the modeled profiles are controlled by the precipitation of illite and sepiolite. The model-predicted dissolved Mg^{2+} concentrations are too low, probably because the Mg content assumed for illite is slightly high (Table 3).

The model predicts that the pore fluid pH should drop sharply with depth below the sediment–water interface to a value of about 7.3 and then decrease gradually with depth to 7.0 at 200 m depth (Fig. 7). The pH measured in pore water extracted from the core is higher (7.7–8.15) and cannot be matched with any reasonable reaction network. A lowering of pH with depth is expected from the production of bicarbonate by sulfate reduction and subsequent calcite precipitation

$$Ca^{2+} + HCO_3^- \rightarrow CaCO_3 + H^+. \quad (20)$$

This pH-lowering effect could only be eliminated if a pH buffering reaction more powerful than the carbonate system were operative. A likely explanation for the discrepancy between the measurements and models is that degassing of CO_2 occurs when the core is brought up to

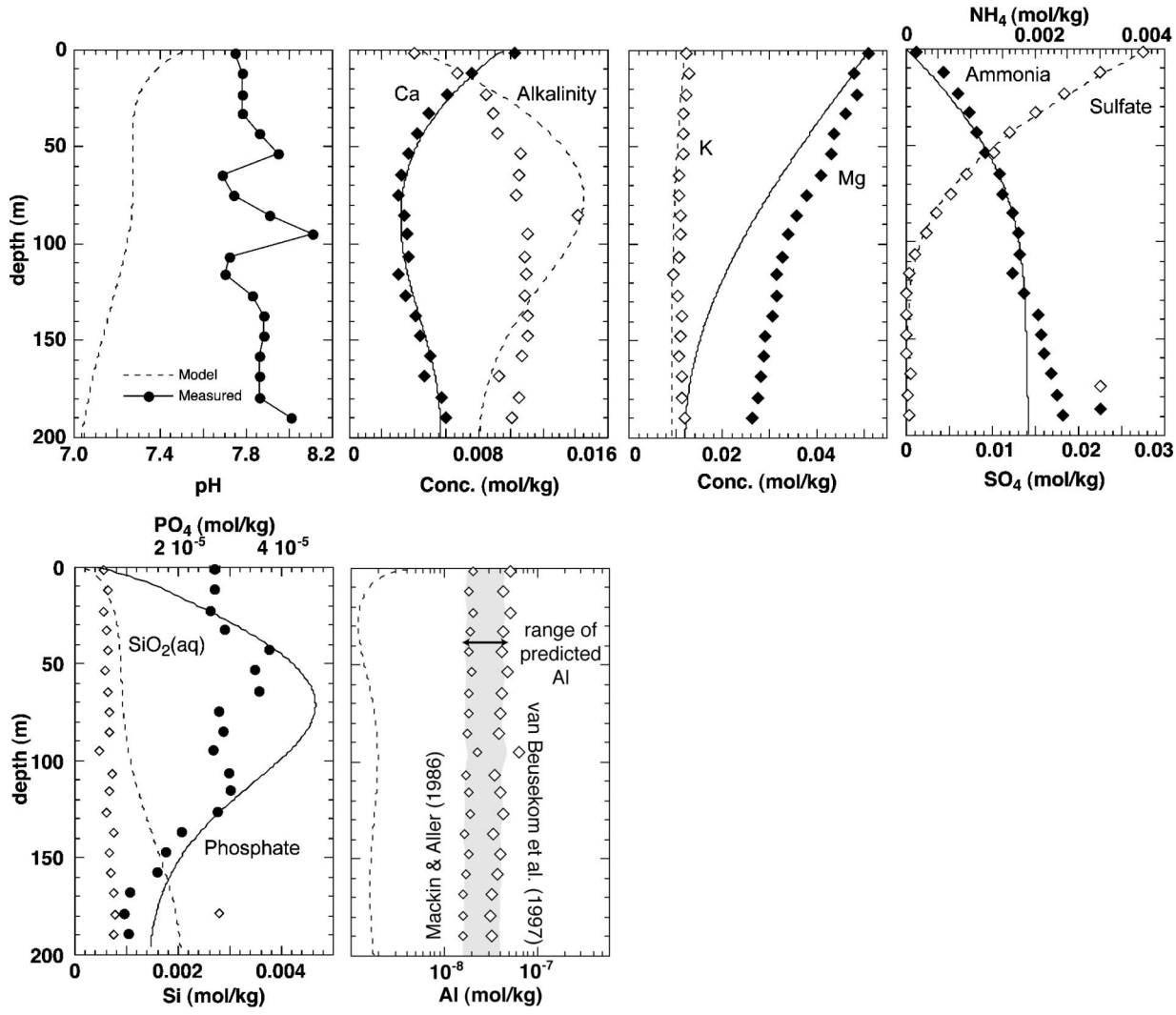

Fig. 7. Measured and modeled concentration profiles using linear TST model. Modeled profiles are shown by solid and stippled lines, and measured data by symbols. Profiles are shown for the best fit to the data using the rate constant/surface area values of $10^{-18.0}$/6.9 m^2/g for plagioclase, smectite at $10^{-18.5}$, illite at 10^{-19}, sepiolite at 10^{-19}, and kaolinite at 10^{-19} mol/m^2/s (all 55 m^2/g). The range of predicted aluminum concentrations (shaded region) is calculated based on the correlation between Al and Si observed in other deep-sea pore water profiles and the Si concentrations measured here (see Appendix 1). Other parameters are given in Tables 3–5.

the surface (the core experiences a drop in total pressure of >160 bar; Giambalvo et al., 2002). The measured values of pH are all close to the average value in surface seawater. Hence, we conclude that the pH measurements are unreliable, which is unfortunate because it removes a potentially useful constraint on the models, and we rely instead on the calculated values.

Alkalinity is also slightly higher in the model than measured in the pore water, although the general trend is captured. The modeled alkalinity increases quite rapidly from 0 to 80 m depth, and reaches a peak of 18 μmol/kg at 80 m, coincident with a peak in measured alkalinity. The profile in the upper half of the core is controlled by anaerobic respiration and calcite precipitation (Fig. 7). Below 80 m, the decrease in modeled alkalinity is caused by siderite precipitation as the availability of H_2S from sulfate reduction is reduced and pyrite precipitation ceases to be the primary removal mechanism for iron.

The lack of aluminum data for the pore water at Site 984 makes it difficult to render a unique and decisive interpretation of the model results. In order to better evaluate the model results, measurements of Al in pore waters from the few pre-existing studies were compiled (Appendix 1). High quality data for aluminum in pore waters are quite sparse, and most of these measurements are confined to the upper few meters of sediment. However, using the linear correlation between Al and Si observed in the external data, a range of expected values for Al can be calculated based on the concentrations of Si in the Site 984 pore water. Using this approximation, we infer a range of Al concentrations of 15–50 nmol/kg (Fig. 7). This range is about a factor of 10 higher than the model results from this scenario, but provides an additional constraint in assessing the relative effects of the different model formulations.

5.3. U isotopic and concentration profiles

Since the concentrations of U in the pore fluid are low (3 nmol/L), and the reactions relatively rapid compared to diffusion, the U isotopic ratios in the pore fluid are sensitive to local conditions (Maher et al., 2004) and hence fluctuate by ±20% over depth intervals of a few meters (Fig. 4A). The small-scale variability of the pore fluid U isotope ratios must reflect corresponding variations in the α-recoil factor, F_α (Eq. (19)), or in the feldspar dissolution rate. In the model, the plagioclase dissolution rate is driven by variations in pore fluid chemistry, which vary smoothly over distances of several tens of meters due to the effects of diffusion in the pore fluid. As a result, the model cannot reproduce the fluctuations in the U isotopic ratios over distances less than about 10 m. Because we do not have data to evaluate variations in F_α with depth, we instead fit the average $^{234}U/^{238}U$ values and evaluate the range of dissolution rates that is compatible with the range of observed $^{234}U/^{238}U$ ratios in both the pore water and carbonate. As shown below, the fluctuations in pore fluid $^{234}U/^{238}U$ ratios correspond to variations in dissolution rate of less than a factor of 2, which is small in comparison to the many order-of-magnitude differences that we are trying to understand.

The modeled uranium concentrations and isotopic profiles are shown in Fig. 8 for plagioclase dissolution rate *constants* corresponding to Eq. (15) ($k_U = 10^{-16.9}$ mol/m^2/s) and for the rate *constant* determined from the major element data of Fig. 7 ($k_f = 10^{-18.0}$ mol/m^2/s). All of these runs assume a linear TST rate law. The modeled $^{234}U/^{238}U$ agrees very well with the measured isotopic data using the rate constant k_U, which was calculated using the approximation of Eq. (15) and hence does not include any dependence on ΔG or possible inhibitory effects. With this rate constant, however, the model pore water U concentrations are exceptionally high and the model is not consistent with the major element chemistry (Fig. 8). When the rate constant, k_f, of $10^{-18.0}$ mol/m^2/s is used, the predicted U concentrations are consistent with the data, but the predicted pore fluid $^{234}U/^{238}U$ is far too high.

The rate constant k_U, which comes from the pore fluid U isotopic ratios, is not strictly applicable to feldspar dissolution because the pore fluid $^{234}U/^{238}U$ values reflect dissolution of all of the U-bearing solid phases, not just feldspar. The other major U-bearing phase in the sediment is calcite. It is reasonable to infer, therefore, that the difference between k_f and k_U is due to calcite recrystallization (Fig. 9). The isotopic data require that there be calcite recrystallization even though the pore fluid is saturated with respect to calcite. The rate of calcite recrystallization, which is a largely isochemical process of dissolution and reprecipitation, can be discerned by considering the isotopic ratios of both the fluid and the calcite, and the total U concentration.

In this particular case, the recrystallization of calcite also provides a net U sink, so that the addition of calcite recrystallization to the model makes the modeled pore fluid U concentration closer to that observed. At a rate of calcite recrystallization (k_r) of $10^{-10.6}$ mol/m^2/s ($\sim 10^{-12.2}$ yr^{-1}), the model reproduces the observed $^{234}U/^{238}U$ of both the pore water and NaOAc leach for the plagioclase dissolution rate determined from the major element data (Fig. 9). This suggests that approximately 10–20 wt. % of the marine calcite is recrystallized by 70 m (Fig. 10).

Maher et al. (2004) attempted to make a rough estimate of the calcite recrystallization rate (and arrived at a value similar to that proposed here), but did not assess the effect

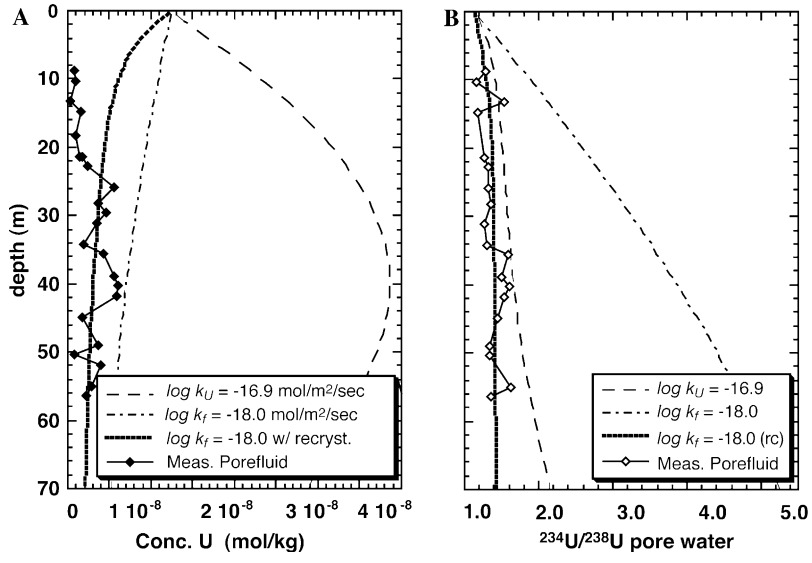

Fig. 8. Comparison of model $^{234}U/^{238}U$ and U concentrations predicted from Eq. (15) and from the major element model (Fig. 7) with no recrystallization. Also shown are model profiles including the effect of recrystallization (dark stippled line). (A) pore water U concentrations for different dissolution rate constants (k_f); (B) comparison of $^{234}U/^{238}U$ profiles for different dissolution rate constants.

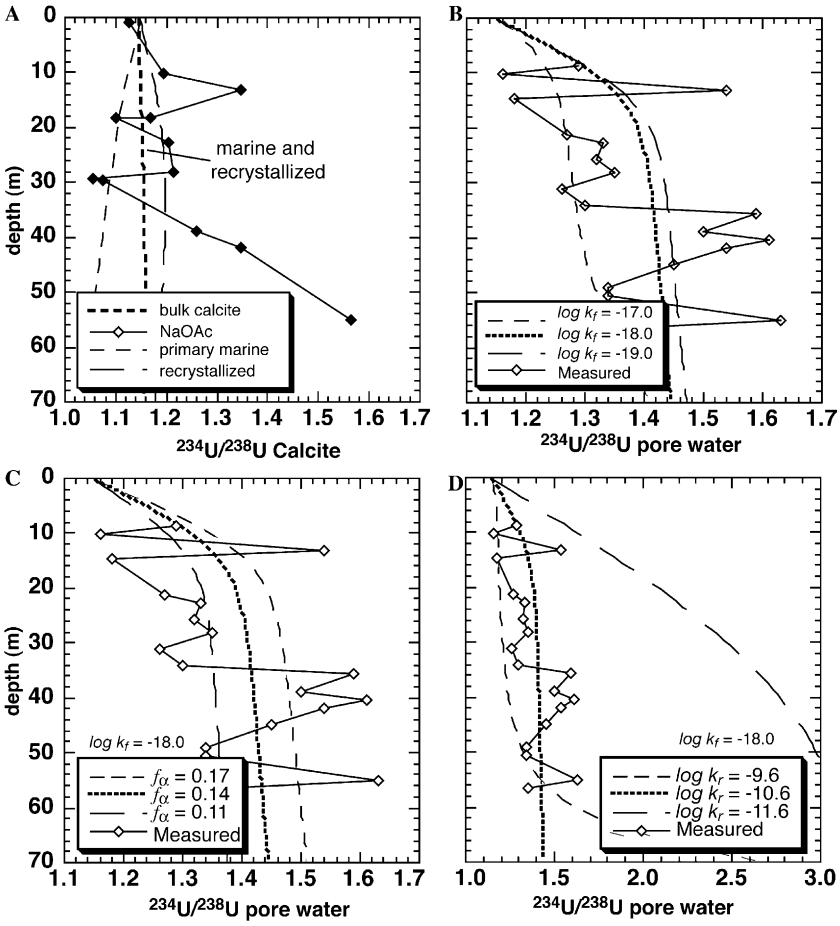

Fig. 9. Calcite and pore water $^{234}U/^{238}U$ as a function of plagioclase dissolution, α-recoil loss, and rate of recrystallization for calcite recrystallization model. (A) bulk calcite (i.e., recrystallized plus primary marine) and recrystallized $^{234}U/^{238}U$ compositions. (B) Effect of variation in plagioclase dissolution rate, (C) effect of recoil loss fraction parameter (f_α), and (D) effect of variation in recrystallization rate.

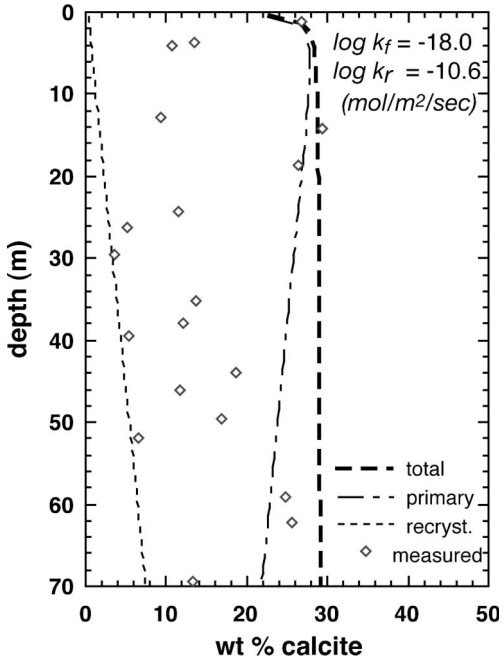

Fig. 10. Model for calcite precipitation and recrystallization showing amount of recrystallized calcite, residual marine calcite, and total calcite.

that this would have on the inferred dissolution rate of silicate phases. Hence, the value of k_U, which was attributed to silicate dissolution by Maher et al. (2004), is actually too high by a factor of 10. The revised value for silicate dissolution needs to be closer to k_f, which in turn makes the discrepancy with laboratory values cited by Maher et al. (2004) larger by a factor of 10 as well.

5.4. Alternative rate law formulations

5.4.1. Parallel rate law formulation

The intrinsic rate constants for feldspar dissolution calculated for Site 984, assuming the parameters and rate laws in the base case scenario, are roughly 5 orders of magnitude slower than those calculated from laboratory studies, and of a similar magnitude to estimates for natural systems of similar age (cf. White and Brantley, 2003). To evaluate the effect of different close-to-equilibrium behavior, the parallel rate law formulation from Fig. 3 (Eqs. (7) and (8)) was implemented. The model was fit to the data by varying the rate constant for plagioclase while maintaining rate constants for other minerals determined from the initial linear TST model the same. The resulting rate con-

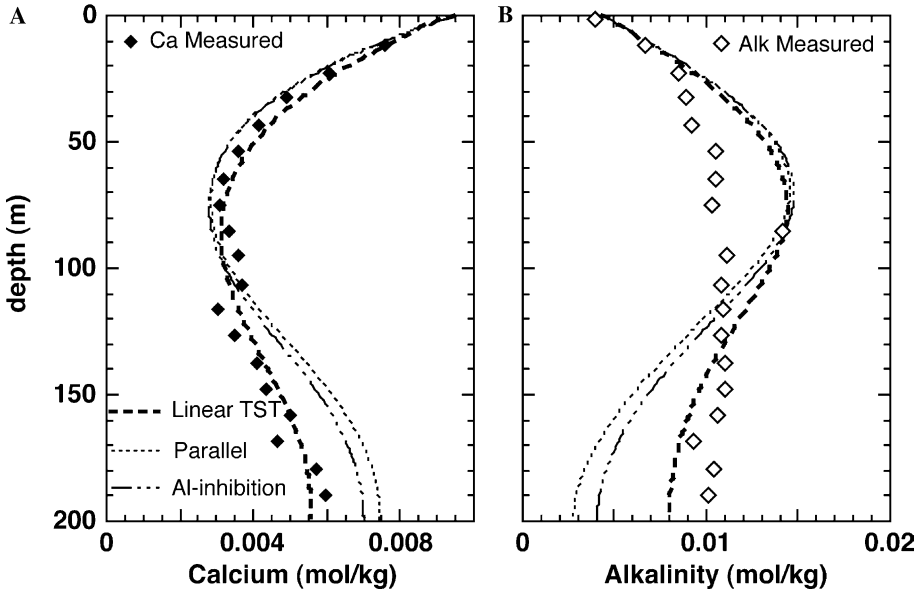

Fig. 11. Comparison of model results for (A) calcium concentrations and (B) alkalinity. Profiles correspond to the base-case TST ($k_f = 10^{-18.0}$ mol/m^2/s), parallel rate law formulation ($k_1 = 10^{-17.8}$; $k_2 = 10^{-16.6}$ mol/m^2/s), and Al-inhibition model ($k_f = 10^{-16.0}$ mol/m^2/s). All other parameters are the same as those for the base case linear TST model from Fig. 7 and Table 5.

stants are $10^{-17.8}$ and $10^{-16.6}$ mol/m^2/s for k_1 and k_2 (Fig. 11). The fit to both the isotopic data and major element data, however, is not as good as for the base case model. The slowing of dissolution with approach to equilibrium that is accounted for in the parallel rate formulation results in a factor of 10 increase in the inferred plagioclase dissolution rate constant. However, the higher rate constant ($k_2 = 10^{-16.6}$ mol/m^2/s) is still 10^4 times smaller than the laboratory value.

5.4.2. Aluminum inhibition

This Al-inhibition rate law was also evaluated using the formulation described in Section 4.6.2 and Appendix 2. In this scenario, a rate constant of $10^{-16.0}$ mol/m^2/s produces the best match of the pore water data assuming a physical (and reactive) surface area of 6.9 m^2/g (Fig. 11). This value for the plagioclase dissolution rate constant is approximately 3 orders of magnitude larger than that inferred using the linear TST model. Total Al concentrations where Al inhibition becomes important are shown in Appendix 2.

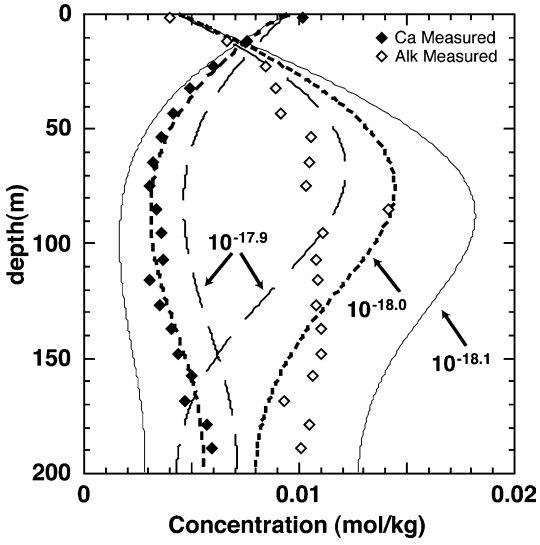

Fig. 12. Sensitivity of model to plagioclase rate constant. Ca^{2+} and alkalinity profiles for different plagioclase rate constants for the linear TST model are shown. Dark stippled line is best-fit ($k_f = 10^{-18.0}$ mol/m^2/s).

6. Discussion

6.1. Interpretation of major element profiles and dissolution rates

The base case fit to the major element data using the linear TST model was obtained for an intrinsic dissolution rate constant of $10^{-18\pm0.9}$ mol/m^2/s for the feldspar assuming a reactive surface area equal to 6.9 m^2/g. The effect of variations in the rate constant value is shown in (Fig. 12). This rate constant can be compared to laboratory-derived kinetic rate constants for albite of the order of $10^{-12.4}$ mol/m^2/s (Knauss and Wolery, 1986). The calculated plagioclase dissolution rate is essentially determined by the concentration of Ca^{2+} in the pore fluid—the Ca^{2+} is apparently the most sensitive indicator of the dissolution rate of the feldspar, although it is affected by calcite precipitation due to the alkalinity produced from sulfate reduction. The alkalinity, which is reduced by the precipitation of calcite, provides a second constraint, which together with the calcium constrains the combined rates of plagioclase dissolution and calcite precipitation.

The calculated saturation states in the model (i.e., $\log \Omega$) for feldspar are between -2 and -3, which is surprising for a rather old system in a neutral pH range (Fig. 13), but is

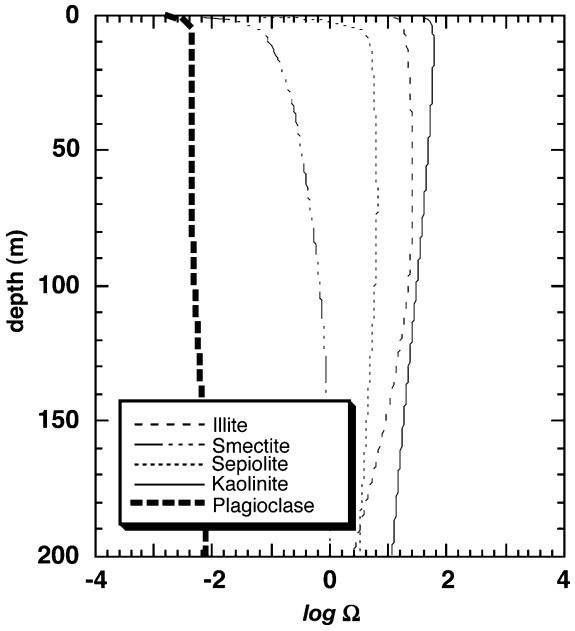

Fig. 13. Computed reaction affinity ($\log\Omega$) for plagioclase, kaolinite, sepiolite, smectite, and illite for the best fit plagioclase rate constant from the linear TST model (Fig. 7) and model parameters shown in Table 5. Actual values could not be computed due to problems in the measurement of aluminum concentrations.

the result of the strong control on fluid chemistry by the biogeochemical reactions and clay precipitation. The corresponding clay precipitation rates are of the order of $10^{-19.0}$ mol/m^2/s assuming a physical surface area equal to the BET values of 55 m^2/g. Variations in the rate constants for clay precipitation could not be precisely constrained beyond the range of approximately 10^{-18} to $10^{-20.5}$ mol/m^2/s. These rates are considerably slower than the few existing kinetic rate constants for precipitation proposed from laboratory studies conducted at higher temperature and lower pH, which are $\sim10^{-10}$ to 10^{-12} mol/m^2/s for kaolinite (Devidal et al., 1997; Nagy et al., 1991, respectively).

The effects of reactive surface area, Al-inhibition, and differing clay solubilities and rates will be considered in the following sections as modifications to the base case model. These analyses are conducted to further explore the relationship between current kinetic theory and observations from a natural system. To reproduce the pore water chemistry for a given model, the product of the individual terms in Eq. (1) must equal approximately the same overall rate as determined from the fit to the major element data from Fig. 7. For example, an increase in the intrinsic rate constant must be balanced by a decrease in the physical surface area, by an inhibition term, or by the reaction affinity term.

6.2. Reactive surface area vs. physical surface area

One explanation offered for inhibited dissolution is that the reactive surface area is much smaller than the total surface area (White and Brantley, 2003). Could the observed slowness of dissolution rates in the Site 984 system relative to laboratory studies be due to a lower reactive surface area, and *not* the intrinsic rate constant? Hydrologic limitation is not a factor in these sediments because of the high porosity, lack of cementation, and diffusion-dominated transport. However, it is possible that authigenic minerals may have armored the feldspar grains, or that given the age of the sediment, significant surface layers have developed which reduce the available surface area. Direct measurement of the physical surface area is made difficult by the small grain size (average of 5–10 μm)—any attempt to separate the minerals would be biased towards the larger grain sizes.

The measurements of the $^{234}U/^{238}U$ in the residual solids provide a unique constraint on the physical surface area of the sediments, because the α-recoil loss fraction for a particle is a function of the ratio of surface area to volume. The depletion of ^{234}U is confined to a surface layer 0.03 μm in thickness, the approximate stopping distance of ^{234}Th in a silicate. Given the estimate of the available surface area (Fig. 5), the physical surface area available for dissolution must be 6.9 ± 1.5 m^2/g. In order for significant secondary armoring or leached layers to reduce the amount of reactive surface area, these layers would have to be much less than 0.03 μm in thickness. To account for the discrepancy observed here, the reactivity of the physical surface area would have to be reduced by 99.99%.

6.3. Aluminum inhibition

Experiments have suggested that aluminosilicate dissolution rates are controlled by the formation and decomposition of an Al-deficient, silica-rich surface precursor complex (Carroll and Knauss, 2005; Devidal et al., 1997; Gautier et al., 1994; Oelkers and Schott, 1995; Oelkers et al., 1994; Wieland and Stumm, 1992). A full evaluation of this model is obviously hindered by the lack of Al data for Site 984 sediments. At a rate constant of $10^{-15.7}$ mol/m^2/s, the predicted Al values are between 2 and 5 nmol/kg, slightly lower than the values selected as the minimum range of likely concentrations (Fig. 16).

The effect of a more soluble plagioclase was also tested using the basalt mineral data of (Stefansson, 2001). The $\log K$ value for the plagioclase dissolution reaction

$$\mathrm{Plag} + 5.988\ \mathrm{H^+} \rightarrow 0.503\ \mathrm{Na^+} + 0.497\ \mathrm{Ca^{2+}} + 1.497\ \mathrm{AlO_2^-} + 2.503\ \mathrm{SiO_{2(aq)}} + 2.994\ \mathrm{H_2O} \qquad (21)$$

was calculated to be −19.95 and −18.81 for 0 and 25 °C, respectively. The increase in solubility of about 2 orders of magnitude did not change the Al and Si concentrations significantly because secondary clay precipitation controls the dissolved Al and Si concentrations. The increase in solubility did change the saturation state of the plagioclase from approximately −2 to −1, however this effect had an insignificant impact on the inferred rate constant.

6.4. Effect of clay minerals on dissolution rate

The previous numerical experiments all suggest that the plagioclase is maintained at a distance from equilibrium of about 1–2 log units. Even a change in the solubility or composition of the plagioclase will not significantly change either the observed rate or the saturation state because of the strong control of the clay minerals on the pore fluid composition (see Appendix 3). Given this relationship, it is instructive to consider the consequences of different assumptions regarding the clay minerals.

Since the overall rate is a product of the terms in Eq. (1), the discrepancy between the rate constants observed in these simulations and those determined from laboratory based measurements could result from a system that is much closer to equilibrium than suggested by the previous simulations. Since the overall rate can be approximated as the product of $k_f(1-\Omega)$, as the reaction affinity decreases the rate constant must increase to maintain the same overall rate. For this mechanism to account for the apparent discrepancy observed here, the $\log\Omega$ for feldspar has to change from the value of approximately -2 predicted in the previous simulations, to a value of approximately 10^{-4}, a much lower value than is measurable in practice. Because Al and Si are removed from solution via precipitation of clays, the precipitation of clay affects the saturation state ($\log\Omega$) of the pore waters with respect to feldspar and consequently the observed dissolution rate constant (Alekseyev et al., 1997). Thus, there are two formulations that can result in a system that is much closer to equilibrium than predicted in our previous simulations: dramatically slower rates of clay precipitation, or a clay composition that is significantly more soluble than the crystalline variety contained in Table 3.

6.4.1. Slow clay model

If clay precipitation rates are slow, the pore water approaches equilibrium with respect to plagioclase, thus slowing its rate of dissolution to match the slow rates of uptake of Si and Al by the clays (Steefel and Van Cappellen, 1990). Using the Al-inhibition formulation from above and the laboratory scale rate constant of Carroll and Knauss (2005), the effect of variation in the clay precipitation rate was assessed. The Al-inhibition formulation was used because as clay precipitation is slowed, the aqueous Al is expected to rise.

The Al-inhibition model used with the laboratory plagioclase rate constant can be made consistent with the measured major element if the clay precipitation rates are extremely slow ($10^{-21.6}$ mol/m^2/s, A of 55 m^2/g). Fig. 14 shows the shift in the saturation state values for the kaolinite and plagioclase, given the "slow clay" model. Slow precipitation of the secondary minerals significantly reduces the inferred rate *constant* of the feldspar because the plagioclase saturation state is very close to equilibrium. This scenario corresponds to Al concentrations that are consistent with our best estimate (upper range), although the Si levels are higher than suggested by the data (Fig. 15). Although it is unlikely that the use of a TST model is ideally suited to describe clay precipitation, the slow clay rates (relative to the base case estimate) result in significant supersaturation with respect to the clay minerals (Fig 14). This consideration, combined with the overprediction of Si, suggest that slow clay precipitation is not sufficient

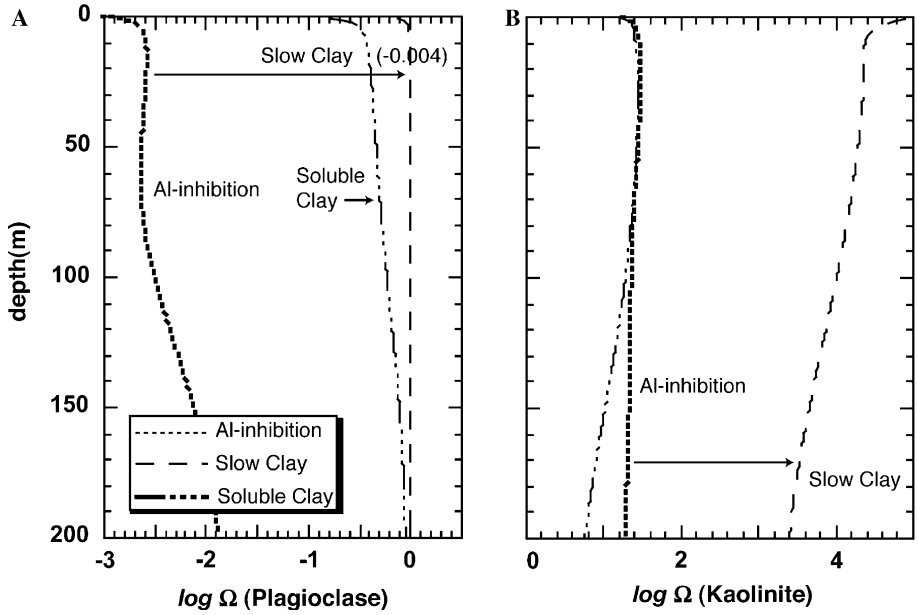

Fig. 14. Comparison of plagioclase and kaolinite reaction affinity ($\log\Omega$) for the Al-inhibition model, given the clay rates determined from the base case scenario, "slow clay" precipitation, and the more soluble clay model. (A) Plagioclase saturation state with $k_f = 10^{-16.0}$ mol/m^2/s, "slow clay" corresponds to k_{clay} of $10^{-21.6}$ mol/m^2/s and the laboratory-derived plagioclase rate constant of $10^{-12.8}$ mol/m^2/s (Carroll and Knauss, 2005), and "soluble clay" represents $\log K$ values that are 4 log units more soluble than the values in Table 5 (other parameters identical to those of an Al-inhibition model). (B) Saturation state for kaolinite with different models for clay precipitation.

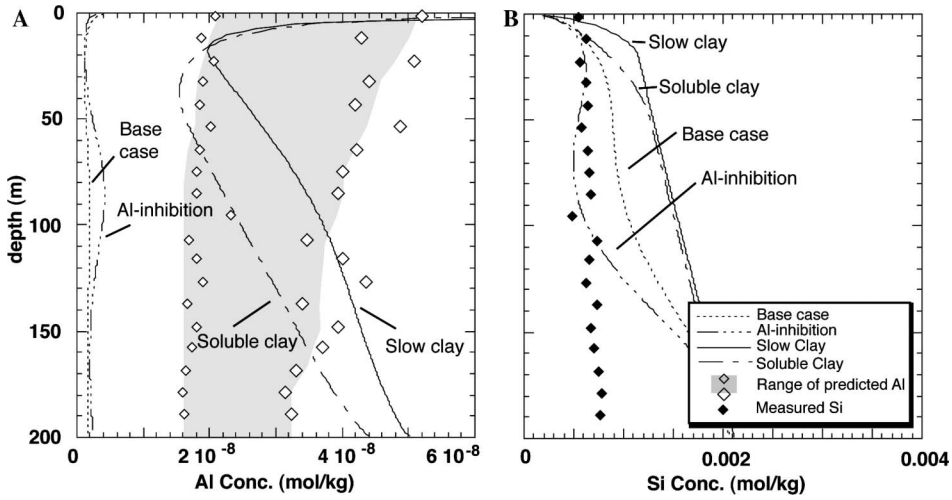

Fig. 15. (A) Model aluminum concentrations and model profiles (note log scale); (B) model silica concentrations and model profiles. The "base case" profile corresponds to the linear TST model (Fig. 7) with $k_f = 10^{-18.0}$ mol/m^2/s,"Al-inhibition" corresponds to k_f of $10^{-16.0}$ mol/m^2/s, and "slow clay" corresponds to k_{clay} of $10^{-21.6}$ mol/m^2/s and the laboratory-derived plagioclase rate constant of $10^{-12.8}$ mol/m^2/s (Carroll and Knauss, 2005). The "soluble clay" model is for log K values that are 4 log units more soluble than the values in Table 5 (other parameters identical to those of an Al-inhibition model).

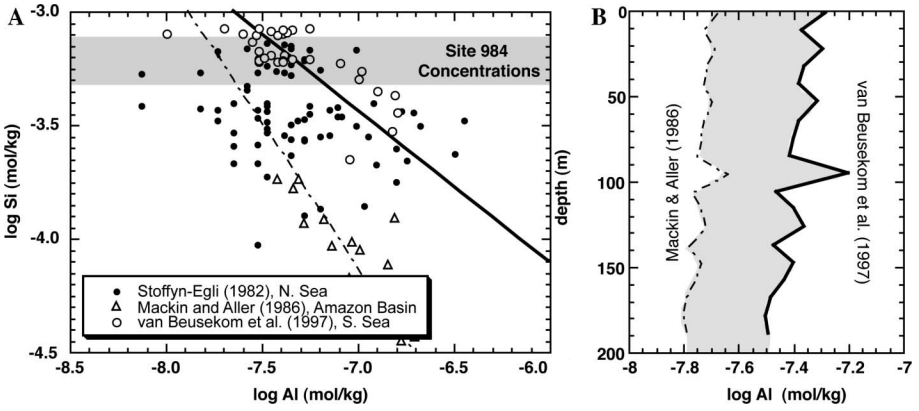

Fig. 16. (A) Existing data from deep-sea pore waters. Solid line is the correlation between the Al and Si data ($R^2 = 0.74$) of Van Beusekom et al. (1997) from the Crozet Basin, South Sea, and light stippled line is the correlation from the Mackin and Aller (1986) measurements ($R^2 = 0.84$); (B) Inferred range of aluminum concentrations based on measured Si concentrations at Site 984 and the correlation with Al shown in (A). Bold line represents the best estimate for Al concentrations.

to explain the entire discrepancy. However, if slow clay precipitation is the reason that plagioclase dissolves so slowly, then it implies that the rate of plagioclase dissolution is almost entirely dependent on the rate of clay precipitation. And since the rates of clay precipitation required to explain the data are about 9 orders of magnitude smaller than the laboratory-measured rates, it simply transfers the problem to one of understanding what controls clay precipitation rates in nature.

6.4.2. More soluble clay model

The seemingly slow rates of clay precipitation may be an artifact of more soluble metastable precursor phases. For example, the saturation state for kaolinite in the slow clay model is ≈4.0. If a more soluble precursor phase such as halloysite is precipitating prior to kaolinite, the *log* Ω value for halloysite could decrease by 1–2 units and the rate constant for precipitation would increase accordingly to maintain the same net rate of removal of Al and Si from the fluid (Steefel and Van Cappellen, 1990).

If the solubility of the clay minerals in the model is increased by 4 orders of magnitude over the crystalline compositions contained in Table 3, the plagioclase rate constant consistent with the data is ≈3 orders of magnitude faster ($10^{-14.9}$ mol/m^2/s). This effect also results from the accumulation of Si and Al in the pore water and results therefore in a lower log Ω value of −0.5 for the plagioclase, while the reaction affinity for the precipitating clays changes only slightly from the previous models (Fig. 14). While the aluminum is in a similar range to our best estimate of what the pore fluid aluminum is (see Appendix 1), the Si is again noticeably higher in this scenario (Fig. 15).

It is also very likely that the kinetic approach used here is not sufficient to describe the complex process of clay

nucleation and precipitation. Without better information regarding the composition and solubilities of the clays and the role of nucleation, or good data on dissolved aluminum concentrations and in situ pH, the above effects are difficult to assess and are meant to illustrate the relationship between secondary mineral precipitation and primary mineral dissolution in natural systems. Attempting to capture the entire discrepancy through variations in the clay minerals results in Si and Al concentrations that are apparently too high. However, these experiments suggest that the kinetics and thermodynamic properties of clay minerals in many natural systems exert significant control over the rate of dissolution of the primary mineral. One conclusion is that dissolution rates in natural systems cannot be completely evaluated without additional information regarding both the saturation state(s) and a detailed composition of the reacting minerals. However, it is essentially impossible to establish if $\log \Omega$ is within 10^{-4} or 10^{-5} of zero, so even if it is theoretically possible to explain slow dissolution rates in terms of small departures from equilibrium, it may be of little practical value for predicting dissolution rates from measurements made on natural systems.

6.5. Origin of the discrepancy between laboratory and field rates

In all of the simulations carried out here, the determination of the dissolution rate of the feldspar is dependent on assumptions regarding clay precipitation. When clay formation does not occur in the model system, plagioclase is predicted to reach equilibrium almost immediately and dissolution ceases. If this were to happen in the real system, the predicted pore fluid Ca^{2+} concentrations would be too low and the alkalinity would be exceedingly high. Other major element profiles and the U isotopic data are also inconsistent with this scenario. If the clay minerals precipitate more rapidly ($\sim > 10^{-18}$ mol/m^2/s) but still slowly, the feldspar is maintained far from equilibrium with the pore fluid and therefore dissolves rapidly. Here, the pore fluid Ca^{2+} becomes exceedingly high, and the alkalinity very low.

The base case linear TST model indicates that plagioclase dissolution rates are so slow that they can be fit only if the laboratory-determined rate *constant* is lowered by ≈5 orders of magnitude, given the reactive surface area assumptions (Table 6). The rate law with a nonlinear dependence on the solution saturation state and the Al-inhibition formulations can account for ≈1.5–2 orders of magnitude of the apparent discrepancy in the feldspar rate constant, with the same clay precipitation rates assumed in the linear TST model. All model formulations suggest an inverse correlation between the plagioclase dissolution rate constant and clay precipitation rates—as the rates of clay precipitation in the model slow, the saturation sate of plagioclase approaches a very small value, and the dissolution rate constant increases. An increase of 4 orders of magnitude in the solubility of the clays, which may reflect the formation of more soluble precursor minerals, also reduces the inferred rate constant by 3 orders of magnitude (Table 6).

According to the calculated α-recoil loss from the sediment, formation of a leached surface layer or armoring by secondary phases do not appear to significantly reduce the physical surface area of the Site 984 sediments. While slow/more soluble clay precipitation may be an important mechanism for moderating feldspar dissolution, it does not provide for more than 3 orders of magnitude in the total discrepancy. A reduction in the intrinsic reactivity of the mineral surfaces during weathering, therefore, is required to explain at least some portion of the 5 order-of-magnitude discrepancy. Recent studies have proposed that with time the surface morphology changes and the number of reactive sites decreases (White and Brantley, 2003). It appears that the Site 984 data are in part explained by a loss of reactive sites on the mineral surface over time, which is consistent with the apparent age-dependence of reaction rates (cf. Maher et al., 2004; White and Brantley, 2003). The observations of naturally weathered minerals suggest that the more reactive surfaces may dissolve first, leaving behind more resistant surface sites (Lee and Parsons, 1995; Van Cappellen and Qiu, 1997). Changes in the nature of the exposed surface area, resulting in a decrease in the number of

Table 6
Comparison of rate constants (mol/m^2/s) determined from laboratory and for Site 984

Model	Percentage of discrepancy[a]	Plagioclase		Illite	Smectite	Kaolinite
		Reference $\log k_f$	Model $\log k_f$[b]	$\log k_f$	$\log k_f$	$\log k_f$
Linear rate law		−12.8[c]	−18.0 ± 0.9	−19 ± 1	−18.5 ± 1	−19 ± 1
Parallel rate law	16	−13.4[d]	−17.8 ± 0.9	−19 ± 1	−18.5 ± 1	−19 ± 1
		−12.2[e]	−16.6 ± 0.9	−19 ± 1	−18.5 ± 1	−19 ± 1
Al-inhibition	41	−12.8[c]	−16.0 ± 0.9	−19 ± 1	−18.5 ± 1	−19 ± 1
Slow clay	100	−12.8[c]	−12.8	−21.6 ± 1	−21.6 ± 1	−21.6 ± 1
Soluble clay	65	−12.8[c]	−14.9 ± 0.9	−19 ± 1	−18.5 ± 1	−19 ± 1

[a] As percentage of difference in log units.
[b] All model rate constants correspond to a reactive surface area of 6.9 m^2/g and units of mol/m^2/s.
[c] Experimental data from Carroll and Knauss (2005) for labradorite.
[d] Corresponds to k_1 from Eq. (7).
[e] Corresponds to k_2 from Eq. (8).

active sites per unit surface area, would be consistent with the observation that fresh mineral surfaces weather more rapidly than natural minerals in the laboratory under the same conditions (Swoboda-Colberg and Drever, 1993; Van Cappellen, 1996; White and Brantley, 2003).

7. Conclusion

The results obtained from modeling of the isotopic and major element profiles at Site 984 suggest that the apparent discrepancy between laboratory and field dissolution rates still exists even when a mechanistic reactive transport model is used to interpret rates in a natural system. For the base case linear TST model, the observed discrepancy is greatest and suggests that the total discrepancy may be as much as 4–5 orders of magnitude. Of the alternative rate laws considered here, such as proximity to equilibrium and Al-inhibition, none are sufficient to remove more than ≈2 orders of magnitude. Changes in the parameters controlling clay precipitation can account for up to ≈3 orders of magnitude in the discrepancy, but large changes in the inferred plagioclase dissolution rate constant occur only if the solubilities and/or precipitation rates of clays are changed by very large (and not necessarily defensible) factors relative to their laboratory-measured values. Therefore, the conclusion from the numerical experiments presented here is that plagioclase dissolution rate constants are smaller than the laboratory-determined rate constants, at least in part, as a result of the reduction in the reactivity of the feldspar surfaces over time. This effect may be accentuated where the minerals experience an extended time at relatively close to equilibrium conditions and is consistent with the observation of the time dependence of natural dissolution rates (Maher et al., 2004; White and Brantley, 2003). One of the implications of our results is that mineral dissolution rates may be controlled largely by the surface properties of the minerals. At present, a major problem is that there is no way to parameterize the reactivity of a surface even if the departure from equilibrium ($\log \Omega$) can be precisely determined. Our results, as well other reports in the literature (e.g., Baxter and DePaolo, 2002), suggest that reactive transport modeling of natural systems will be highly uncertain until there is means to estimate the intrinsic reactivity of a surface from measurements of natural materials.

The reactive transport simulations also indicate that the precipitation of secondary minerals sustains the dissolution of the plagioclase, which implies that an analysis of silicate mineral dissolution rates in natural systems must factor in the rates and/or solubilities of secondary phases.

The major element and isotopic methods predict similar dissolution rate constants if additional lowering of the pore water $^{234}U/^{238}U$ activity ratio is attributed to isotopic exchange via recrystallization of marine calcite, which makes up about 10–20% of the Site 984 sediment. The incorporation of the U-data into the model provides a constraint on overall rates of reaction, but may have difficulty in distinguishing between different reactions. In this regard, the U isotopic data, in combination with the major element profiles, suggest that exchange with the pore water and calcite is an important effect that cannot be attributed to precipitation alone, but requires a recrystallization mechanism. Reactive transport modeling of U isotopes combined with the major element chemistry, therefore, provides a useful means of quantifying the extent of recrystallization and tracking its effect on the sedimentary record.

The results from Site 984 also highlight the important link between the biogeochemical and inorganic reaction pathways. The production of alkalinity via sulfate reduction drives calcite precipitation, while the dissolution of feldspar provides additional calcium to the system to sustain the observed dissolved Ca profiles and persistent (but slow) calcite precipitation. The precipitation of clay minerals, in addition to moderating the dissolution rate of feldspar, controls the pH and alkalinity by acting as a sink for H^+. While the biogeochemical reactions will operate in the absence of the silicate system, components such as the carbonate system, the $Fe(OH)_3$–H_2S system, and the alkalinity are also linked to the dissolution/precipitation of the aluminosilicate minerals. In addition, the dynamic exchange of aqueous species between dissolving and precipitating phases as a result of recrystallization may have significant consequences for the diagenetic record.

Acknowledgments

This research was supported by the SEGRF Fellowship, University of California/Lawrence Livermore National Laboratory, and the Director, Office of Science, Basic Energy Sciences, Chemical Sciences, Biosciences and Geosciences Division of the U.S. Department of Energy under Contract No. De-AC03-76SF00098 in the form of separate grants to the second and third authors. We gratefully acknowledge the associate editor and the many reviewers for their insightful comments on earlier varsions of this manuscript.

Associate editor: Eric. H. Oelkers

Appendix 1. Derivation of rate law for Al-inhibition

Oelkers et al. (1994) proposed that the dissolution of plagioclase is controlled by the rate of detachment of a silica-rich precursor complex (M–$SiOH_{3n}$) on the mineral surface:

$$r_+ = k_+(\text{M–SiOH}_{3n}), \tag{A.1}$$

where k_+ is the rate constant for the elementary detachment reaction. The silica-rich precursor is formed under slightly acidic conditions according to the fast (equilibrium) reaction

$$\text{M–}n\text{AlSiO} + 3n\text{H}^+ \Longleftrightarrow \text{M–SiOH}_{3n} + n\text{Al}^{3+}, \tag{A.2}$$

where n is the number of moles of Al in the surface site M–nAlSiO. As with any equilibrium reaction, one can write a mass action equation

$$K_f = \frac{[\text{M–SiOH}_{3n}][\text{Al}^{3+}]^n}{[\text{M–}n\text{AlSiO}][\text{H}^+]^{3n}}, \quad (A.3)$$

where the square brackets [ ] refer to the activities of the dissolved and surface species. The reaction can be rewritten in terms of the species $Al(OH)_3$, which makes the expression of the rate law slightly easier from a computational point of view. If this is done, the formation constant, K_f, can be transformed simply by multiplying through by mass action equation for the aluminum hydrolysis reaction

$$K'_f = K_f K^n_{\text{Al(OH)}_3} = \frac{[\text{M–SiOH}_{3n}][\text{Al(OH)}_3]^n}{[\text{M–}n\text{AlSiO}]}. \quad (A.4)$$

We can now solve for the concentration of the silica-rich precursor

$$[\text{M–SiOH}_{3n}] = \frac{K'_f[\text{M–}n\text{AlSiO}]}{[\text{Al(OH)}_3]^n}, \quad (A.5)$$

and then eliminate the concentration of Al-rich precursor by noting that the total reactive sites S, is given by the sum of the Al-rich and Si-rich precursor species

$$S = [\text{M–}n\text{AlSiO}] + [\text{M–SiOH}_{3n}]. \quad (A.6)$$

If we assume that the activities of the surface species are equal to their concentrations, we obtain

$$\text{M–SiOH}_{3n} = \frac{K'_f(S - \text{M–SiOH}_{3n})}{[\text{Al(OH)}_3]^n}. \quad (A.7)$$

At this point, there are two ways to proceed algebraically. One way is to write

$$\text{M–SiOH}_{3n}\left(1 + \frac{K'_f}{[\text{Al(OH)}_3]^n}\right) = \frac{SK'_f}{[\text{Al(OH)}_3]^n}, \quad (A.8)$$

$$\text{M–SiOH}_{3n} = \frac{\frac{SK'_f}{[\text{Al(OH)}_3]^n}}{\left(1 + \frac{K'_f}{[\text{Al(OH)}_3]^n}\right)}, \quad (A.9)$$

which is similar to Eq. (14) in Oelkers et al. (1994), except for the conversion to the neutral aqueous species $Al(OH)_3$. Alternatively, we can multiply by the activity of $Al(OH)_3$:

$$\text{M–SiOH}_{3n}[\text{Al(OH)}_3]^n = K'_f(S - \text{M–SiOH}_{3n}), \quad (A.10)$$

$$\text{M–SiOH}_{3n}\left([\text{Al(OH)}_3]^n + K'_f\right) = K'_f S, \quad (A.11)$$

$$\text{M–SiOH}_{3n} = S\frac{K'_f}{\left([\text{Al(OH)}_3]^n + K'_f\right)}. \quad (A.12)$$

This allows us to define the rate of the Si-rich precursor complex detachment reaction using Eq. (A.1) as:

$$r_+ = k_+ S\frac{K'_f}{\left([\text{Al(OH)}_3]^n + K'_f\right)} = k_f\frac{K'_f}{\left([\text{Al(OH)}_3]^n + K'_f\right)}, \quad (A.13)$$

where the rate constant, k_f (mol m^{-2} s^{-1}), is defined as the product of the elementary rate constant, k_+, and the total number of reactive sites on the feldspar surface (S). This form of the rate law, although mathematically identical to that proposed by Oelkers et al. (1994) and Carroll and Knauss (2005), has the advantage that it demonstrates clearly the hyperbolic form of the dissolved aluminum inhibition term (compare to the inhibition term used in microbial kinetics, Eq. (5)). Eq. (A.13) states that inhibition by dissolved aluminum will be negligible where the activity of the species $[\text{Al(OH)}_3]^n << K'_f$ (Fig. 17). The activity of the aqueous species $Al(OH)_3$ can of course be related to the total dissolved aluminum with a knowledge of the pH. An approximate measure of where inhibition of the feldspar dissolution reaction by dissolved aluminum is important is given by the case where $[\text{Al(OH)}_3] = (K'_f)^{1/n}$. Where this is the case, the rate of dissolution will be 1/2 of its maximum value, r_{max}, which is achieved when no inhibition by dissolved aluminum occurs. Values of the total dissolved aluminum corresponding to this case ($r_+ = 1/2r_{max}$) as a function of pH for a temperature of 25 °C are given in Fig. 17. In this calculation, as in the reactive transport calculations discussed in the text, we use a value of $n = 1/3$, which is close to the fitted value of 0.31 determined by Carroll and Knauss (2005).

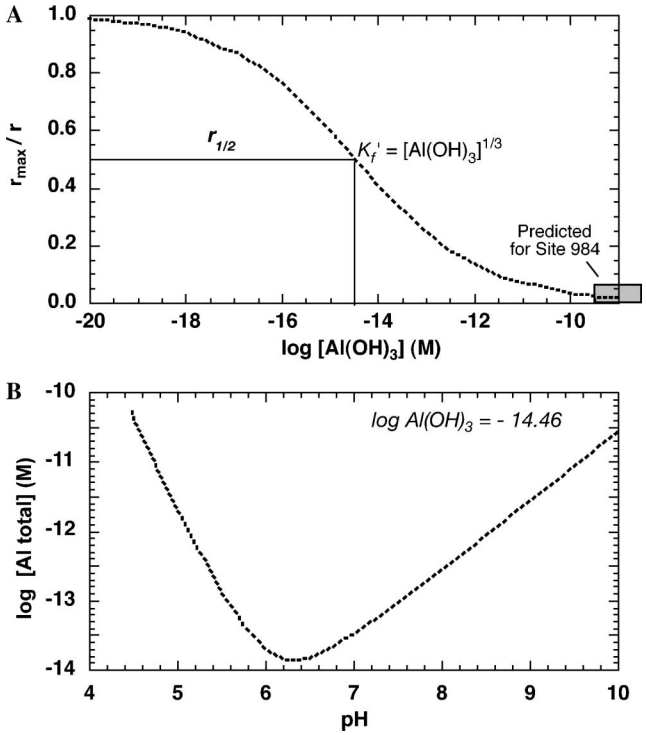

Fig. 17. (A) Effect of $Al(OH)_3$ concentrations on overall rate (r). The rate is half of the maximum value (r_{max}) where $\log[\text{Al(OH)}_3]$ is equal to $3\log K'_f$ or −14.46 (where $\log K'_f = -4.82$). (B) Total Al as a function of pH at the value of $\log K'_f$ determined by Carroll and Knauss (2005) (converted from Al^{3+} to $Al(OH)_3$). This corresponds to the total concentration of Al in the pore water where the $r = 0.5\ r_{max}$.

Appendix 2. Predicted pore water aluminum concentrations

Aluminum measurements for Site 984 pore water were attempted. However, the excessively high concentrations (average 100 μmol/L) suggested that the samples were most

likely contaminated during extraction, handling or storage. However, dissolved Al and Si in sediment pore waters commonly exhibit an inverse relationship (Caschetto and Wollast, 1979; Mackin and Aller, 1984, 1986; Stoffyn-Egli, 1982; Van Beusekom et al., 1997). To define a range of expected values for Site 984 pore waters, measurements for Al and Si concentrations from other deep-sea pore waters were compiled and plotted (Fig. 16). The Mackin and Aller (1986) data are from pore waters in silicate-rich sediments in the Amazon Basin and the Van Beusekom et al. (1997) measurements are from sediments with high contents of biogenic silica (~18 wt. %) in the South Sea. The data from Stoffyn-Egli (1982) from the North Atlantic fall within the trends delineated by the aforementioned data sets.

Using measured pore water data from Mackin and Aller (1986) and Van Beusekom et al. (1997), a predictive model for Al concentrations as a function of total dissolved Si was constructed for each data set (Fig. 16A). These correlations bracket the range of observed Al and Si values. The linear correlations (shown in Fig. 16A) were then used in conjunction with the measured Si concentrations at Site 984 to estimate a range of likely Al concentrations (Fig. 16B). The profile predicted from the Van Beusekom et al. (1997) correlation is shown in dark stippled lines, and lower range is determined from the correlation between Al and Si observed by Mackin and Aller (1986). These profiles may be biased towards higher Al concentrations because in some cases the Al was beneath the detection limit for the analytical technique. These values, which are highly uncertain, do provide an additional framework for evaluating model results in a relative sense.

Appendix 3. Evaluation of model uncertainty

3.1. Uncertainty in the U-series model architecture

The U isotopic model provides an additional constraint on the dissolution of plagioclase. However, there are also considerable assumptions inherent in this method of approximating mineral dissolution rates in this system. The model assumes that the pore water U is dominantly contributed by the plagioclase and marine calcite via dissolution and recrystallization, *and* is only consumed by the calcite via precipitation. Variations in the U content of the plagioclase have a minimal effect on the predicted $^{234}U/^{238}U$ profiles because F_α also depends on the concentration of U in the plagioclase. It is likely that some fraction of the U is contained within other phases not directly considered here, such as phosphorites, amorphous silica, and other silicate minerals. Of the silicate minerals that could also be dissolving, the most likely phases are Mg-rich silicates such as amphibole, olivine, and pyroxene, K-feldspar, and volcanic glass. Volcanic glass derived from Iceland volcanics most likely dissolved prior to deposition or early on the depositional sequence. The concentration of uranium in the aforementioned Mg-silicate minerals is in general less than in the feldspars (Blundy and Wood, 2003), and these minerals were not observed in substantial amounts in the XRF measurements for the Site 984 sediments, thus the contribution of U from dissolution of other silicate minerals is likely to be minimal. In addition, because none of these minerals are likely to contain either significant amounts of uranium or dramatically different isotopic compositions from the plagioclase, the potential for one or two phases to dramatically impact the system is minimal.

Of the secondary minerals, clay minerals, SiO_2(am), iron–sulfides, and phosphorites (primarily carbonate fluorapatite and apatite) are known to contain appreciable U (Andersson et al., 2001; Barnes and Cochran, 1990; Fuller et al., 2002; Thomson et al., 1990). Relative to $CaCO_3$ the majority of these minerals are expected to have a minimal effect on the removal of U from solution but may be important in systems where the calcite influence is smaller. Because clay precipitation is pervasive with depth, the incorporation of U into the clay minerals would not affect the isotopic ratio of the fluid, but may reduce the aqueous uranium concentrations slightly The assumptions in the U-series components that introduce the most error into the model are therefore the assumptions regarding the concentration and $^{234}U/^{238}U$ of the dissolving feldspar and the precipitated/recrystallized calcite, and the volume fraction of plagioclase in the sediment.

3.2. Uncertainty in major element model architecture

Aside from the lack of pore water Al data and precise mineralogy, there are several assumptions that introduce uncertainty into the above models, including the composition of the dissolving/precipitating phases and the solubility of the minerals. The composition of the plagioclase represents the best approximation of the average value of all plagioclase in the sediments. Subtle variations in the composition and thus the solubility of the minerals are most likely present. An increase in the solubility of the feldspar for the same ratio of anorthite/albite did not substantially affect the model results because of the moderating effect of clay precipitation on the plagioclase dissolution rate. However, changes in the An/Ab composition of the mineral, notably the Ca concentration, may affect the perceived rate constants because Ca was the primary determinant for agreement between model and data. The difference in $\log K$ (25 °C) values between plagioclase with a composition of $An_{70}Ab_{30}$ and $An_{29}Ab_{71}$ is of the order of 0.02 log units (Stefansson, 2001). The above compositions ($An_{70}Ab_{30}$ and $An_{29}Ab_{70}$) resulted in minimal change to the calculated rate constants (±0.05 log units) apparently because the increase in solubility for the high-anorthite mineral was offset by the decrease in Ca, and vice versa for the high-albite mineral. The additional uncertainties resulting from the above considerations, and errors associated with the pore water measurements and modeled pH are

included with the best estimates of the rate constants from each model in Table 6.

References

Alekseyev, V.A., Medvedeva, L.S., Prisyagina, N.I., Meshalkin, S.S., Balabin, A.I., 1997. Change in the dissolution rates of alkali feldspars as a result of secondary mineral precipitation and approach to equilibrium. *Geochim. Cosmochim. Acta* **61** (6), 1125–1142.

Andersson, P.S., Porcelli, D., Gustafsson, O., Ingri, J., Wasserburg, G.J., 2001. The Importance of colloids for the behavior of uranium isotopes in the low-salinity zone of a stable estuary. *Geochim. Cosmochim. Acta* **65** (1), 13–25.

Barnes, C.E., Cochran, J.K., 1990. Uranium removal in oceanic sedimentation and the oceanic balance. *Earth Plan. Sci. Let.* **97**, 94–101.

Baxter, E.F., DePaolo, D., 2002. Field measurement of high temperature bulk reaction rates II: Interpretation of results from a field site near Simplon Pass, Switzerland. *Am. J. Sci.* **302** (6), 465–516.

Berner, R.A., 1977. Stoichiometric models for nutrient regeneration in anoxic sediments. *Limnol. Oceanogr.* **22** (5), 781–786.

Berner, R.A., 1980. *Early Diagenesis: A Theoretical Approach*. Princeton University Press, Princeton, NJ.

Biscaye, P.E., 1965. Mineralogy and sedimentation of recent deep-sea clay in Atlantic Ocean and adjacent seas and oceans. *Geol Soc. Am. Bull.* **76** (7), 803.

Blum, A.E., Lasaga, A.C., 1991. The role of surface speciation in the dissolution of albite. *Geochim. Cosmochim. Acta* **55** (8), 2193–2201.

Blundy, J., Wood, B., 2003. Mineral-melt partitioning of uranium, thorium and their daughters. In: *Uranium-Series Geochemistry*, vol. 52, pp. 59–123.

Brantley, S.L., Blai, A.C., Cremeens, D.L., Macinnis, I., Darmody, R.G., 1993. Natural etching rates of feldspar and hornblende. *Aquat. Sci.* **55** (4), 262–272.

Burch, T.E., Nagy, K.L., Lasaga, A.C., 1993. Free-energy dependence of albite dissolution kinetics at 80 °C and pH 8.8. *Chem. Geol.* **105** (1–3), 137–162.

Busenberg, E., Plummer, L.N., 1989. Thermodynamics of magnesian calcite solid-solutions at 25 °C and 1-atm total pressure. *Geochim. Cosmochim. Acta* **53** (6), 1189–1208.

Cagatay, M.N., Borowski, W.S., Ternois, Y.G., 2001. Factors affecting the diagenesis of Quaternary sediments at ODP Leg 172 sites in western North Atlantic: evidence from pore water and sediment geochemistry. *Chem. Geol.* **175** (3–4), 467–484.

Cama, J., Ganor, J., Ayora, C., Lasaga, C.A., 2000. Smectite dissolution kinetics at 80 °C and pH 8.8. *Geochim. Cosmochim. Acta* **64** (15), 2701–2717.

Carroll, S., Knauss, K.G., 2005. Dependence of labradorite dissolution kinetics on CO_2(aq), Al(aq), and temperature. *Chem. Geol.* **217**, 213–225.

Carter, S.J., Raymo, M.E., 1999. Sedimentological and mineralogical control of multisensor track data at Sites 981 and 984. In: Raymo, M.E., Jansen, E., Blum, P., Herbert, T.D. (Eds.), *Proceedings of the Ocean Drilling Program, Scientific Results*, vol. 162. Ocean Drilling Program, pp. 247–257.

Caschetto, S., Wollast, R., 1979. Dissolved aluminum in interstitial waters of recent marine-sediments. *Geochim. Cosmochim. Acta* **43** (3), 425–428.

Channell, J.E.T., Lehmen, B., 1999. Magnetic stratigraphy of North Atlantic Sites 980–984. In: Raymo, M.E., Jansen, E., Blum, P., Herbert, T.D. (Eds.), *Proceedings of the Ocean Drilling Program, Scientific Results*, vol. 162. Ocean Drilling Project, pp. 113–130.

Chen, Y., Brantley, S.L., 1997. Temperature- and pH-dependence of albite dissolution rate at acid pH. *Chem. Geol.* **135** (3–4), 275–290.

Chou, L., Wollast, R., 1984. Study of the weathering of albite at room-temperature and pressure with a fluidized-bed reactor. *Geochim. Cosmochim. Acta* **48** (11), 2205–2217.

Cole, T.G., 1985. Composition, oxygen isotope geochemistry, and origin of smectite in the metalliferous sediments of the Bauer Deep, Southeast Pacific. *Geochim. Cosmochim. Acta* **49** (1), 221–235.

de Lange, G.J., 1992. Distribution of exchangeable, fixed, organic and total nitrogen in interbedded turbiditic pelagic sediments of the Madeira Abyssal-Plain, Eastern North-Atlantic. *Mar. Geol.* **109** (1–2), 95–114.

Delanghe, D., Bard, E., Hamelin, B., 2002. New TIMS constraints on the uranium-238 and uranium-234 in seawaters from the main ocean basins and the Mediterranean Sea. *Mar. Chem.* **80**, 79–93.

Devidal, J.L., Schott, J., Dandurand, J.L., 1997. An experimental study of kaolinite dissolution and precipitation kinetics as a function of chemical affinity and solution composition at 150 °C, 40 bar, and pH 2, 6.8, and 7.8. *Geochim. Cosmochim. Acta* **61** (24), 5165–5186.

Dove, P.M., 1995. Kinetic and thermodynamic controls on silica reactivity in weathering environments. In: *Chemical Weathering Rates of Silicate Minerals*, vol. 31, pp. 235–290.

Drever, J.I., Clow, D.W., 1995. Weathering rates in catchments. In: White, A.F., Brantley, S.L. (Eds.), *Chemical Weathering Rates of Silicate Minerals*, vol. 31. Mineralogical Society of America.

Fleischer, R.L., 1982. Alpha-recoil damage and solution effects in minerals - uranium isotopic disequilibrium and radon release. *Geochim. Cosmochim. Acta* **46** (11), 2191–2201.

Fleischer, R.L., 1988. Alpha-recoil damage—relation to isotopic disequilibrium and leaching of radionuclides. *Geochim. Cosmochim. Acta* **52** (6), 1459–1466.

Fuller, C.C., Bargar, J.R., Davis, J.A., Piana, M.J., 2002. Mechanisms of uranium interactions with hydroxyapatite: Implications for groundwater remediation. *Environ. Sci. Technol.* **36** (2), 158–165.

Gautier, J.M., Oelkers, E.H., Schott, J., 1994. Experimental-study of K-feldspar dissolution rates as a function of chemical affinity at 150 °C and pH-9. *Geochim. Cosmochim. Acta* **58** (21), 4549–4560.

Giambalvo, E.R., Steefel, C.I., Fisher, A.T., Rosenberg, N.D., Wheat, C.G., 2002. Effect of fluid-sediment reaction on hydrothermal fluxes of major elements, eastern flank of the Juan de Fuca Ridge. *Geochim. Cosmochim. Acta* **66** (10), 1739–1757.

Gout, R., Oelkers, E.H., Schott, J., Zwick, A., 1997. The surface chemistry and structure of acid-leached albite: new insights on the dissolution mechanism of the alkali feldspars. *Geochim. Cosmochim. Acta* **61** (14), 3013–3018.

Hall, I.R., Measures, C.I., 1998. The distribution of Al in the IOC stations of the North Atlantic and Norwegian Sea between 52 degrees and 65 degrees North. *Mar. Chem.* **61** (1–2), 69–85.

Harvey, C., Gorelick, S.M., 2000. Rate-limited mass transfer or macrodispersion: which dominates plume evolution at the Macrodispersion Experiment (MADE) site? *Water Resour. Res.* **363**, 637–650.

Henderson, G.M., Onions, R.K., 1995. U-234/U-238 Ratios in Quaternary Planktonic-Foraminifera. *Geochim. Cosmochim. Acta* **59** (22), 4685–4694.

Hochella, M.F., Banfield, J.F., 1995. Chemical weathering of silicates in nature: a microscopic perspective with theoretical considerations*Chemical Weathering Rates of Silicate Minerals*, vol. 31. Mineralogical Society of America, pp. 353–406.

Hover, V.C., Walter, L.M., Peacor, D.R., 2002. K uptake by modern estuarine sediments during early marine diagenesis, Mississippi Delta Plain, Louisiana, USA. *J. Sediment. Res.* **72** (6), 775–792.

Hunter, K.S., Wang, Y.F., Van Cappellen, P., 1998. Kinetic modeling of microbially-driven redox chemistry of subsurface environments: coupling transport, microbial metabolism and geochemistry. *J. Hydrol.* **209** (1–4), 53–80.

Hussain, N., Krishnaswami, S., 1980. U-238 series radioactive disequilibrium in groundwaters—implications to the origin of excess U-234 and fate of reactive pollutants. *Geochim. Cosmochim. Acta* **44** (9), 1287–1291.

Iversen, N., Jorgensen, B.B., 1993. Diffusion-coefficients of sulfate and methane in marine-sediments—influence of porosity. *Geochim. Cosmochim. Acta* **57** (3), 571–578.

Karpoff, A.M., Destrigneville, C., Bartier, D., Dejardin, P., 2002. Phyllosilicates and zeolite assemblages in the carbonate periplatform of the Great Bahama Bank: origin and relation to diagenetic processes (ODP Leg 166, Sites 1006 and 1007). *Mar. Geol.* **185** (1–2), 55–74.

Kigoshi, K., 1971. Alpha-recoil thorium-234—dissolution into water and uranium-234/uranium-238 disequilibrium in nature. *Science* **173** (3991), 47–49.

Kim, K., 2002. Plagioclase weathering in the groundwater system of a sandy, silicate aquifer. *Hydrol. Processes* **16** (9), 1793–1806.

Knauss, K.G., Wolery, T.J., 1986. Dependence of albite dissolution kinetics on pH and time at 25 °C and 70 °C. *Geochim. Cosmochim. Acta* **50** (11), 2481–2497.

Kohler, S.J., Dufaud, F., Oelkers, E.H., 2003. An experimental study of illite dissolution kinetics as a function of pH from 1.4 to 12.4 and temperature from 5 to 50°C. *Geochim. Cosmochim. Acta* **67** (19), 3583–3594.

Ku, T.L., 1976. Uranium-series methods of age-determination. *Annu. Rev. Earth Planet. Sci.* **4**, 347–379.

Kump, L.R., Brantley, S.L., Arthur, M.A., 2000. Chemical, weathering, atmospheric CO_2, and climate. *Annu. Rev. Earth Planet. Sci.* **28**, 611–667.

Lakshtanov, L.Z., Stipp, S.L.S., 2004. Experimental study of europium(III) coprecipitation with calcite. *Geochim. Cosmochim. Acta* **68** (4), 819–827.

Langmuir, D., 1997. *Aqueous Environmental Geochemistry*. Prentice Hall.

Lasaga, A.C., Luttge, A., 2001. Variation of crystal dissolution rate based on a dissolution stepwave model. *Science* **291** (5512), 2400–2404.

Lasaga, A.C., Soler, J.M., Ganor, J., Burch, T.E., Nagy, K.L., 1994. Chemical-weathering rate laws and global geochemical cycles. *Geochim. Cosmochim. Acta* **58** (10), 2361–2386.

Lee, M.R., Parsons, I., 1995. Microtextural controls of weathering of perthitic alkali feldspars. *Geochim. Cosmochim. Acta* **59** (21), 4465–4488.

Lei, C., Garrels, R.M., Wollast, R., 1989. Comparative-study of the kinetics and mechanisms of dissolution of carbonate minerals. *Chem. Geol.* **78** (3–4), 269–282.

Lewis, E., Wallace, D., 1998. Program Developed for CO_2 System Calculations. Oak Ridge National Laboratory, Oak Ridge, Tennessee. ORNL/CDIAC-105.

Li, Y.H., Gregory, S., 1974. Diffusion of ions in sea-water and in deep-sea sediments. *Geochim. Cosmochim. Acta* **38** (5), 703–714.

Luo, S.D., Ku, T.L., Roback, R., Murrell, M., McLing, T.L., 2000. In situ radionuclide transport and preferential groundwater flows at INEEL (Idaho). *Decay-series Disequilibrium Studies* **64** (5), 867–881.

Mackin, J.E., Aller, R.C., 1984. Dissolved Al in sediments and waters of the east China Sea—implications for authigenic mineral formation. *Geochim. Cosmochim. Acta* **48** (2), 281–297.

Mackin, J.E., Aller, R.C., 1986. The effects of clay mineral reactions on dissolved Al distributions in sediments and waters of the Amazon Continental-Shelf. *Cont. Shelf Res.* **6** (1–2), 245–262.

Maher, K., DePaolo, D.J., Lin, J.C.F., 2004. Rates of silicate dissolution in deep-sea sediment: in situ measurement using U-234/U-238 of pore fluids. *Geochim. Cosmochim. Acta* **68** (22), 4629–4648.

Malmstrom, M.E., Destouni, G., Banwart, S.A., Stromberg, B.H.E., 2000. Resolving the scale-dependence of mineral weathering rates. *Environ. Sci. Technol.* **34** (7), 1375–1378.

Meece, D.E., Benninger, L.K., 1993. The coprecipitation of Pu and other radionuclides with $CaCO_3$. *Geochim. Cosmochim. Acta* **57** (7), 1447–1458.

Michalopoulos, P., Aller, R.C., 1995. Rapid clay mineral formation in Amazon Delta sediments—reverse weathering and oceanic elemental cycles. *Science* **270** (5236), 614–617.

Michalopoulos, P., Aller, R.C., 2004. Early diagenesis of biogenic silica in the Amazon delta: alteration, authigenic clay formation, and storage. *Geochim. Cosmochim. Acta* **68** (5), 1061–1085.

Murray, R.W., Miller, D.J., Krye, K.A., 2000. *Analysis of Major and Trace Elements in Rocks, Sediments, and Interstitial Waters by Inductively Coupled Plasma-Atomic Emission Spectroscopy (ICP-AES)*. Ocean Drilling Project, College Station, TX.

Nagy, K.L., Blum, A.E., Lasaga, A.C., 1991. Dissolution and precipitation kinetics of kaolinite at 80 °C and pH 3—the dependence on solution saturation state. *Am. J. Sci.* **291** (7), 649–686.

Oelkers, E.H., Schott, J., 1995. Experimental study of anorthite dissolution and the relative mechanism of feldspar hydrolysis. *Geochim. Cosmochim. Acta* **59** (24), 5039–5053.

Oelkers, E.H., Schott, J., Devidal, J.L., 1994. The effect of aluminum, pH, and chemical affinity on the rates of aluminosilicate dissolution reactions. *Geochim. Cosmochim. Acta* **58** (9), 2011–2024.

Raymo, M.E., Jansen, E., Blum, P., Herbert, T.D. 1999. *Proceedings of the Ocean Drilling Program, Scientific Results*. Ocean Drilling Program.

Richter, F.M., DePaolo, D.J., 1987. Numerical-models for diagenesis and the neogene Sr isotopic evolution of seawater from DSDP Site 590b. *Earth Planet. Sci. Lett.* **83** (1–4), 27–38.

Richter, F.M., Liang, Y., 1993. The rate and consequences of Sr diagenesis in deep-sea carbonates. *Earth Planet. Sci. Lett.* **117** (3–4), 553–565.

Robinson, L.F., Belshaw, N.S., Henderson, G.M., 2004. U and Th concentrations and isotope ratios in modern carbonates and waters from the Bahamas. *Geochim. Cosmochim. Acta* **68** (8), 1777–1789.

Schrag, D.P., Adkins, J.F., McIntyre, K., Alexander, J.L., Hodell, D.A., Charles, C.D., McManus, J.F., 2002. The oxygen isotopic composition of seawater during the Last Glacial Maximum. *Quat. Sci. Rev.* **21** (1–3), 331–342.

Soetaert, K., Herman, P.M.J., Middelburg, J.J., 1996. A model of early diagenetic processes from the shelf to abyssal depths. *Geochim. Cosmochim. Acta* **60** (6), 1019–1040.

Steefel, C.I., 2001. Software for modeling multicomponent, multidimensional reactive transport. Lawrence Livermore National Laboratory,Livermore, Ca. UCRL-MA-143182.

Steefel, C.I., Lasaga, A.C., 1994. A coupled model for transport of multiple chemical-species and kinetic precipitation dissolution reactions with application to reactive flow in single-phase hydrothermal systems. *Am. J. Sci.* **294** (5), 529–592.

Steefel, C.I., Lichtner, P.C., 1998. Multicomponent reactive transport in discrete fractures: I. Controls on reaction front geometry. *J. Hydrol.* **209** (1–4), 186–199.

Steefel, C.I., Van Cappellen, P., 1990. A new kinetic approach to modeling water–rock interaction—the role of nucleation, precursors, and Ostwald Ripening. *Geochim. Cosmochim. Acta* **54** (10), 2657–2677.

Steefel, C.I., Yabusaki, S.B., 1996. *OS3D/GIMRT, Software for Multicomponent-Multidimensional Reactive Transport: User's Manual and Programmer's Guide*. Pacific Northwest National Laboratory, Richland, Washington. PNNL-11166.

Stefansson, A., 2001. Dissolution of primary minerals of basalt in natural waters—I. Calculation of mineral solubilities from 0 to 350 °C. *Chem. Geol.* **172** (3–4), 225–250.

Stoffyn-Egli, P., 1982. Dissolved aluminum in interstitial waters of recent terrigenous marine-sediments from the North-Atlantic Ocean. *Geochim. Cosmochim. Acta* **46** (8), 1345–1352.

Swoboda-Colberg, N.G., Drever, J.I., 1993. Mineral dissolution rates in plot-scale field and laboratory experiments. *Chem. Geol.* **105** (1–3), 51–69.

Taylor, A., Blum, J.D., 1995. Relation between soil age and silicate weathering rates determined from the chemical evolution of a glacial chronosequence. *Geology* **23** (11), 979–982.

Taylor, A.S., Blum, J.D., Lasaga, A.C., 2000. The dependence of labradorite dissolution and Sr isotope release rates on solution saturation state. *Geochim. Cosmochim. Acta* **64** (14), 2389–2400.

Teichert, B.M.A., Eisenhauer, A., Bohrmann, G., Haase-Schramm, A., Bock, B., Linke, P., 2003. U/Th systematics and ages of authigenic carbonates from Hydrate Ridge, Cascadia Margin: recorders of fluid flow variations. *Geochim. Cosmochim. Acta* **67** (20), 3845–3857.

Tessier, A., Campbell, P.G.C., Bisson, M., 1979. Sequential extraction procedure for the speciation of particulate trace-metals. *Anal. Chem.* **51** (7), 844–851.

Thomson, J., Wallace, H.E., Colley, S., Toole, J., 1990. Authigenic uranium in Atlantic sediments of the Last Glacial Stage—a diagenetic phenomenon. *Earth Planet. Sci. Lett.* **98** (2), 222–232.

Van Beusekom, J.E.E., Van Bennekom, A.J., Treguer, P., Morvan, J., 1997. Aluminium and silicic acid in water and sediments of the Enderby and Crozet Basins. *Deep-Sea Res. II* **44** (5), 987–1003.

Van Cappellen, P., 1996. Reactive surface area control of the dissolution kinetics of biogenic silica in deep-sea sediments. *Chem. Geol.* **132** (1–4), 125–130.

Van Cappellen, P., Gaillard, J.F., 1996. Biogeochemical dynamics in aquatic sediments. In: Lichtner, P.C., Steefel, C.I., Oelkers, E.H. (Eds.), *Reactive Transport in Porous Media*, vol. 34, pp. 335–371.

Van Cappellen, P., Qiu, L.Q., 1997. Biogenic silica dissolution in sediments of the Southern Ocean—2. Kinetics. *Deep-Sea Res. II* **44** (5), 1129–1149.

Wang, Y.F., Van Cappellen, P., 1996. A multicomponent reactive transport model of early diagenesis: application to redox cycling in coastal marine sediments. *Geochim. Cosmochim. Acta* **60** (16), 2993–3014.

White, A.F., 1995. Chemical weathering rates of silicate minerals in soils. In: *Chemical Weathering Rates of Silicate Minerals*, vol. 31, Mineralogical Society of America, pp. 407–461.

White, A.F., Blum, A.E., Schulz, M.S., Bullen, T.D., Harden, J.W., Peterson, M.L., 1996. Chemical weathering rates of a soil chronosequence on granitic alluvium. 1. Quantification of mineralogical and surface area changes and calculation of primary silicate reaction rates. *Geochim. Cosmochim. Acta* **60** (14), 2533–2550.

White, A.F., Brantley, S.L., 2003. The effect of time on the weathering of silicate minerals: why do weathering rates differ in the laboratory and field? *Chem. Geol.* **202** (3–4), 479–506.

White, A.F., Peterson, M.L., 1990. Role of reactive-surface-area characterization in geochemical kinetic-models. *ACS Symp. Ser.* **416**, 461–475.

Wieland, E., Stumm, W., 1992. Dissolution kinetics of kaolinite in acidic aqueous-solutions at 25 °C. *Geochim. Cosmochim. Acta* **56** (9), 3339–3355.

Wieland, E., Werhli, B., Stumm, W., 1988. The coordination chemistry of weathering: 3. A potential generalization on dissolution rates of minerals. *Geochim. Cosmochim. Acta* **52**, 1969–1981.

Wijsman, J.W.M., Herman, P.M.J., Middelburg, J.J., Soetaert, K., 2002. A model for early diagenetic processes in sediments of the continental shelf of the Black Sea. *Estuar. Coast. Shelf Sci.* **54** (3), 403–421.

Wolery, T.J., Jackson, K.J., Bourcier, W.L., Bruton, C.J., Viani, B.E., Knauss, K.G., Delany, J.M., 1990. Current Status of the EQ3/6 Software Package for Geochemical Modeling. *ACS Symp. Ser.* **416**, 104–116.

Wolfram, S., 2003. *Mathematica* 5.0. Wolfram Research, Inc.

Wright, A.K., Flower, B.P., 2002. Surface and deep ocean circulation in the subpolar North Atlantic during the mid-Pleistocene revolution. *Paleoceanography* **17** (4).

Yao, W.S., Millero, F.H., 1995. Oxidation of hydrogen sulfide by Mn(IV) and Fe(III) (hydr)oxides in seawater. In: *Geochemical Transformations of Sedimentary Sulfur*, vol. 612, pp. 260–279.

Yao, W.S., Millero, F.J., 1996. Oxidation of hydrogen sulfide by hydrous Fe(III) oxides in seawater. *Mar. Chem.* **52** (1), 1–16.

Zhu, C., 2005. In situ feldspar dissolution rates in an aquifer. *Geochim. Cosmochim. Acta* **69** (6), 1435–1453.